

Emergent complex phases in a discrete flocking model with reciprocal and non-reciprocal interactions

Matthieu Mangeat,^{1,*} Swarnajit Chatterjee,^{1,†} Jae Dong Noh,^{2,‡} and Heiko Rieger^{1,§}

¹*Center for Biophysics & Department for Theoretical Physics,
Saarland University, 66123 Saarbrücken, Germany.*

²*Department of Physics, University of Seoul, Seoul 02504, Korea.*

We have undertaken a comprehensive study of the two-species active Ising model (TSAIM), a discrete-symmetry counterpart of the continuous-symmetry two-species Vicsek model [Phys. Rev. E **107**, 024607 (2023)], motivated by recent interest in the impact of complex and heterogeneous interactions on active matter systems. In the TSAIM, two species of self-propelled particles undergo biased diffusion in two dimensions, interacting via local alignment/anti-alignment. Our investigation explores both reciprocal and non-reciprocal interactions between the two species, along with the possibility of species interconversion. In the reciprocal TSAIM, we observe a liquid-gas phase transition, exhibiting macrophase-separated bands, and the emergence of a high-density parallel flocking state, a feature not seen in previous flocking models. With species interconversion (species-flip dynamics), the TSAIM corresponds to an active extension of the Ashkin-Teller model and exhibits a broader range of steady-state phases, including microphase-separated bands that further enrich the coexistence region. In the non-reciprocal TSAIM, a novel run-and-chase dynamics emerges. We also find that the system is metastable due to droplet excitation and exhibits spontaneous motility-induced interface pinning, preventing the system from reaching long-range order at sufficiently low noise. A hydrodynamic theory complements our computer simulations of the microscopic model and confirms the reported phase diagrams.

I. INTRODUCTION

Active matter is a class of natural or synthetic non-equilibrium systems composed of many agents that consume energy to move or exert mechanical forces. Over the past two decades, intensive research has established active matter as a significant field of study [1–6], with assemblies of active particles exhibiting complex behaviors and collective effects, such as the emergence of large, ordered clusters known as flocks. Flocking plays a significant role in a wide range of systems across disciplines including physics, biology, ecology, social sciences, and neurosciences [7] and is an out-of-equilibrium phenomenon abundantly observed in nature [1, 4–6].

A widely studied computational model for flocking is the celebrated Vicsek model (VM) [8, 9]. In this model, point particles with rotational symmetry tend to align with their neighbors while moving at a fixed speed. This alignment is not perfect as particles make error which are modeled as a stochastic noise. Although the VM shows a transition from a disordered (low-density, high-noise) to an ordered (high-density, low-noise) phase, Solon et al. [10, 11] demonstrated that this is better understood as a liquid-gas transition with a phase-separated coexistence region for intermediate noise and density. Remarkably, despite its continuous symmetry, the VM exhibits true long-range order in two dimensions, seemingly vio-

lating the Mermin-Wagner theorem, which prohibits the spontaneous breaking of continuous symmetry in two-dimensional systems in thermal equilibrium. However, as Toner and Tu [12] showed through their hydrodynamic theory, this apparent violation arises because the moving flock operates far from equilibrium. The non-equilibrium nature of the system, driven by the motion of particles, allows for the emergence of macroscopic order and the breaking of rotational invariance.

Subsequently, the active Ising model (AIM) [13] was introduced which replaces the continuous rotational symmetry of the VM with a discrete symmetry, while preserving the essential physics of the VM. The AIM exhibits three steady-states similar to the VM: disordered gas at high noise and low densities, polar liquid at low noise and high densities, and a phase-separated liquid-gas coexistence region at intermediate densities and temperatures. The key distinction between the VM and the AIM is that the former exhibits giant density fluctuations leading to microphase separation of the coexistence region, while the latter shows normal density fluctuations resulting in bulk phase separation. Recent studies on the q -state active Potts model (APM) [14] and the q -state active clock model (ACM) [15] have provided further insights into flocking transitions. These models have emerged as more generalized frameworks for flocking bridging the VM and the AIM.

Due to their inherent out-of-equilibrium nature, active systems exhibit long-range order (LRO) [8] and survive spin wave fluctuations [12]. Consequently, it was thought that polar-ordered phases in the active matter are generally robust to fluctuations. In addition, studies of these flocking models are typically conducted in idealized settings, assuming perfectly identical particles in an infi-

*Electronic address: mangeat@lusi.uni-sb.de

†Electronic address: swarnajit.chatterjee@uni-saarland.de

‡Electronic address: jdnoh@uos.ac.kr

§Electronic address: heiko.rieger@uni-saarland.de

nite and homogeneous environment. However, real flocks are more complex, and recent studies have revealed that even a single small obstacle or artificially excited droplet within the ordered phase can destabilize it, as observed in the VM [16, 17]. This contrasts sharply with passive systems, where such a small perturbation typically only induces a local effect. Furthermore, these perturbations can emerge spontaneously and this spontaneous fluctuation could similarly destabilize the ordered phase, as recently observed in the constant-density Toner-Tu flocks [18] and the AIM [19, 20], where ordered flocks become metastable over large time scales, eventually transitioning to a disordered state.

Additionally, the models of self-propelled particles mostly focus on homogeneous systems where every agent has exactly the same dynamical properties and follows the same “rules of engagement”. However, heterogeneity is ubiquitous in nature and complex systems are typically heterogeneous as individuals have disparate characteristics and vary in their properties [21, 22]. In particular, many biological systems that show flocking involve self-propelled particles with heterogeneous interactions which can significantly impact system dynamics, as seen in studies of mixed bacterial populations [23–25]. Theoretically, various aspects of heterogeneous systems of self-propelled agents have been investigated. For example, alignment interactions in a binary mixture of self-propelled particles have shown that different interaction potentials can lead to parallel, antiparallel, or perpendicular alignment, resulting in diverse collective motion patterns [26]. Other investigations have explored particles with varying velocities [27], noise sensitivity [22, 28], sensitivity to external cues [29], and particle-to-particle interactions [30]. Different self-propelled particle species were also analyzed in predator-prey scenarios [31, 32] and in the context of reciprocal, e.g. the two-species Vicsek model (TSVM) [33], as well as non-reciprocal interactions [34, 35].

The TSVM [33], which is a two-species extension of the VM with reciprocal antiferromagnetic interspecies interactions, exhibits two primary steady states describing the collective motion: the anti-parallel flocking (APF) state, where the two species form bands moving in opposite directions, and the parallel flocking (PF) state, where the bands travel in the same direction. In the low-density and high-noise part of the coexistence region, PF and APF states perform fluctuation-induced stochastic transitions from one to the other where the transition frequency decreases with increasing system size. Furthermore, the PF state vanishes at high densities and low noises, leaving the APF state as the only ordered *liquid* phase.

Finally, an increasing number of recent studies involving non-equilibrium systems have focused on how non-reciprocal interactions in active matter affect non-equilibrium phase transitions and drive the emergence of states or patterns in active matter [6]. A non-reciprocal interaction violates Newton’s third law “actio=reactio” and leads to frustration between two elements due to

their opposing objectives. In soft matter systems, non-reciprocity arises when interparticle forces are mediated by a non-equilibrium environment, leading to the emergence of novel self-organized states dependent on time [34, 36–38]. More prominent, if not ubiquitous, are non-reciprocal interactions in active and living systems that break detailed balance at the microscale, from social forces [39] and neural networks [40, 41] to antagonistic interspecies interactions in bacteria [42], cells [43] and predator-prey systems [44]. In contrast to equilibrium systems governed by Newton’s third law, non-reciprocal systems are generally considered to be out of equilibrium [45] and therefore non-reciprocal interactions are associated with a gain or a loss of energy. Although the incorporation of non-reciprocal interactions is not required to capture flocking behavior, there is a recent push toward understanding the effects of non-reciprocal interaction on the phase behavior of flocking objects [34, 35, 46, 47].

In this paper, we investigate a two-species variant of the active Ising model (AIM) [13], namely the two-species active Ising model (TSAIM), which serves as a discrete-symmetry counterpart to the continuous-symmetry TSVM [33]. In the TSAIM, self-propelled particles from two distinct *species* A and B undergo biased diffusion in two dimensions along with local alignment. In this context, we have mainly considered three different scenarios: (a) reciprocal TSAIM with conserved species where a particle aligns with particles of the same species and anti-aligns with particles of the other species but the population of each species remains conserved, (b) reciprocal TSAIM with non-conserved species where the alignment protocol follows (a) but a particle of one species can convert to the other species, and (c) non-reciprocal TSAIM with conserved species where, while particles of the same species tend to align with their species, particles of different species interact in a non-reciprocal manner: A particles tend to align with B, while the B particles tend to anti-align with the particles of species A.

This paper is organized as follows: we introduce the model and simulation details in Sec. II and Sec. III presents the hydrodynamic theory of the system. In Sec. IV, we discuss the results obtained for reciprocal interactions without species flip, followed by Sec. V, where we present the results with reciprocal interactions including species flip. Sec. VI focuses on our findings with the non-reciprocal interactions. Finally, we summarize and conclude our findings in Sec. VII.

II. MODEL AND SIMULATION DETAILS

A. Microscopic model

We consider an ensemble of N particles in a periodic two-dimensional square lattice of size $L_x \times L_y$. The average particle density is $\rho_0 = N/L_x L_y$. The j^{th} particle on site i is equipped with a spin-orientation $\sigma_i^j = \pm 1$ which

determines the biased hopping with self-propulsion ε via the rate:

$$W_{\text{hop}}(\sigma, \mathbf{p}) = D(1 + \theta\varepsilon|\mathbf{p} \cdot \mathbf{e}_x| + \sigma\varepsilon\mathbf{p} \cdot \mathbf{e}_x), \quad (1)$$

with $\theta \in [0, 1]$, i.e. a rate $W_+ = D[1 + (\theta + 1)\varepsilon]$ in the favored direction ($\mathbf{p} = \sigma\mathbf{e}_x$), a rate $W_- = D[1 + (\theta - 1)\varepsilon]$ in the unfavored direction ($\mathbf{p} = -\sigma\mathbf{e}_x$), and a constant rate D in the upward and downward directions ($\mathbf{p} = \pm\mathbf{e}_y$). The parameter $0 \leq \varepsilon \leq 1/(1 - \theta)$ controls the asymmetry between the non-motile limit $\varepsilon = 0$ ($W_+ = W_- = D$) and the limit where the particle never jumps to the unfavored direction $\varepsilon = 1/(1 - \theta)$ ($W_- = 0$). On average, a particle drifts with speed $v = 2D\varepsilon$ in the direction set by the sign of its spin orientation, and diffuses with diffusion constant $D_{xx} = D + \theta v/2$ and $D_{yy} = D$ along x and y directions, respectively. The total hopping rate thus becomes $4D + \theta v$, and the limiting values in ε give the inequality $v \leq 2D/(1 - \theta)$. The case $\theta = 0$, i.e. $W_{\pm} = D(1 \pm \varepsilon)$, will be used to derive the main results, as in Ref. [13], while the case $\theta = 1$, i.e. $W_- = D$ and $W_+ = D + v$, will be used to study the stability of the liquid state, as in Refs. [19, 20], since the diffusion D can be made small in comparison to the velocity v .

The particle is further equipped with a species degree of freedom $s_i^j = \pm 1$ which defines the particle species ($s_A = 1$ and $s_B = -1$). The number of particles on site i , with spin orientation σ and species spin s is denoted by $n_{s,i}^\sigma$. No restriction is applied to the number of particles of species s on site i : $\rho_{s,i} = \sum_{\sigma} n_{s,i}^\sigma$ and to the total number of particles on site i : $\rho_i = \rho_{A,i} + \rho_{B,i}$. The local magnetization of species s on site i is defined by: $m_{s,i} = \sum_{j \in s} \sigma_i^j = n_{s,i}^+ - n_{s,i}^-$.

Analogous to the one-species AIM [13], we consider the following flipping rate for a particle with spin σ and species s on site i , for an inverse temperature β :

$$W_{\text{flip}}^{(1)}(\sigma \rightarrow -\sigma) = \gamma_1 \exp\left(-\frac{2\beta}{\rho_i} \sigma J_{ss'} m_{s',i}\right), \quad (2)$$

where the Einstein notation is used: $J_{ss'} m_{s',i} = J_{sA} m_{A,i} + J_{sB} m_{B,i}$. Here, $J_{ss'}$ represents the coupling constant of species s' acting on species s .

First, we consider reciprocal interactions between the two species. Similar to the TSVM [33], the coupling constant is given by $J_{ss'} = J_1 s s'$ (with $J_1 > 0$), which is positive when the two species are the same (ferromagnetic interaction) and negative when the species are different (anti-ferromagnetic interaction). We can now define the following two key order parameters [33]: the total local magnetization

$$v_{s,i} = \sum_j \sigma_i^j = m_{A,i} + m_{B,i}, \quad (3)$$

defining the average propulsion direction at site i , and

the local magnetization difference

$$v_{a,i} = \sum_j s_i^j \sigma_i^j = m_{A,i} - m_{B,i}, \quad (4)$$

playing the role of the order parameter of the ferromagnetic interaction. From Eq. (2), the flipping rate for the spin-orientation in the reciprocal TSAIM then becomes:

$$W_{\text{flip}}^{(1)}(\sigma \rightarrow -\sigma) = \gamma_1 \exp\left(-\frac{2\beta J_1}{\rho_i} s \sigma v_{a,i}\right). \quad (5)$$

Note that, this expression is similar to the one-species flipping rate [13], with $v_{a,i}$ replacing the one-species magnetization.

In the case of non-reciprocal interactions between species, we primarily focus on the scenario where $J_{AA} = J_{BB} = J_1$ and $J_{AB} = -J_{BA} = J_{\text{NR}} \leq J_1$. From Eq. (2), the flipping rate for the spin-orientation in the non-reciprocal TSAIM is defined as the following:

$$W_{\text{flip}}^{(1)}(\sigma \rightarrow -\sigma) = \gamma_1 \exp\left(-\frac{2\beta J_1}{\rho_i} \sigma \mu_{s,i}\right), \quad (6)$$

where $\mu_{s,i} = m_{s,i} + s(J_{\text{NR}}/J_1)m_{-s,i}$ plays the role of order parameter for species s . We also investigate a more general coupling constant such that $-J_1 \leq J_{BA} \leq 0 \leq J_{AB} \leq J_1$, where species A interacts ferromagnetically with species B, while species B has an anti-ferromagnetic interaction with species A.

Additionally, the spins s_i^j defining the particle species may interact locally on site i , via an Ising interaction independent of the spin-orientation of the particles. As for the one-species AIM, we consider the following flipping rate for the species-spin in the TSAIM:

$$W_{\text{flip}}^{(2)}(s \rightarrow -s) = \gamma_2 \exp\left(-\frac{2\beta J_2}{\rho_i} s m_i\right), \quad (7)$$

where the coupling constant J_2 of species-species interactions is positive, and $m_i = \sum_j s_i^j = \rho_{A,i} - \rho_{B,i}$ is the species magnetization on site i . We define $m_0 = (N_A - N_B)/L_x L_y$ as the average species magnetization at the initial time.

The reciprocal TSAIM with species flip ($\gamma_2 \neq 0$) is a natural *active* extension of the well-known Ashkin-Teller (AT) model [48], in which four components interact, equivalent to two coupled Ising-like subsystems (here coupling spins σ and species s) [49]. The order parameters $\langle v_s \rangle \sim \langle \sigma \rangle$, $\langle m \rangle \sim \langle s \rangle$, and $\langle v_a \rangle \sim \langle \sigma s \rangle$ measure the relative ordering between the spins and species [50].

It is crucial to emphasize that three separate magnetizations are explicitly defined at each site i in this model: (i) the magnetization of species A, denoted $m_{A,i} = \sum_{j \in A} \sigma_i^j$, (ii) the magnetization of species B, denoted $m_{B,i} = \sum_{j \in B} \sigma_i^j$, and (iii) the species magnetization, denoted $m_i = \sum_j s_i^j$. The state of the site i is completely defined by these three magnetizations and

the total density ρ_i . In the following, we will consider $\rho_i \equiv \rho(x_i, y_i)$, $m_i \equiv m(x_i, y_i)$, $\rho_{s,i} \equiv \rho_s(x_i, y_i)$, and $m_{s,i} \equiv m_s(x_i, y_i)$, as equivalent expressions where (x_i, y_i) are the coordinates of the site i .

B. Simulation details

We perform Monte Carlo simulations which evolve in discrete time steps of length Δt . At each time step, N randomly chosen particles are updated. A particle can either hop with a probability $p_{\text{hop}} = (4D + \theta v)\Delta t$, or flip its spin orientation with a probability $p_{\text{flip}}^{(1)} = W_{\text{flip}}^{(1)}\Delta t \leq \exp(2\beta J_1)\Delta t$, or flip its species with a probability $p_{\text{flip}}^{(2)} = W_{\text{flip}}^{(2)}\Delta t \leq \exp(2\beta J_2)\Delta t$. The probability that nothing happens during this single particle update is $p_{\text{wait}} = 1 - p_{\text{hop}} - p_{\text{flip}}^{(1)} - p_{\text{flip}}^{(2)}$. An expression for Δt can be chosen to minimize the value of p_{wait} :

$$\Delta t = \frac{1}{4D + \theta v + \gamma_1 \exp(2\beta J_1) + \gamma_2 \exp(2\beta J_2)}. \quad (8)$$

This hybrid dynamics combines Monte Carlo and real-time dynamics previously used in the simulations of the one-species AIM [13]. Without any loss of generality, we take $\gamma_1 = 1$, and we denote $\beta_1 \equiv \beta J_1 = T_1^{-1}$ and $\beta_2 \equiv \beta J_2 = T_2^{-1}$ playing the role of two effective inverse temperatures for the spin-spin and species-species interactions, respectively.

We primarily consider square and rectangular domains with periodic boundary conditions in x and y -direction to compute the steady-state density profiles and state diagrams. Simulations are performed for several control parameters: the average density ρ_0 , the self-propulsion parameter ε , and the different effective temperatures or coupling constants (T_1 and T_2 in the case of reciprocal interactions, J_{AB} , J_{BA} and $T_1 \equiv \beta_1^{-1}$ in case of non-reciprocal interactions). We consider several initial conditions: (a) a disordered configuration with random initial positions (x_i, y_i) and random spin-orientations σ ; (b) a semi-ordered configuration where A and B particles are arranged in two high-density bands, either in a parallel flock (PF) state ($\sigma_A = \sigma_B$) or an anti-parallel flock (APF) state ($\sigma_A = -\sigma_B$); (c) an ordered configuration with random initial positions but with spin-orientations chosen to form a PF or APF state. Depending on the studied case, the initial population of A and B species can be either $m_0 = 0$ or $m_0 = \rho_0$. The maximum time t_{max} to reach a steady state is approximately $t_{\text{max}}/\Delta t \sim 10^5 - 10^7$ Monte Carlo steps (MCS). The C++ codes used for numerical simulations are available in Ref. [51].

III. HYDRODYNAMIC EQUATIONS

In this section, we will derive the hydrodynamic equations from the microscopic update rules elaborated in

Sec. II. From the average particle density $\rho_s^\sigma(\mathbf{x}; t) \equiv \langle n_s^\sigma(\mathbf{x}; t) \rangle$ in state σ and species s , at position \mathbf{x} and time t , we define the particle density $\rho_s(\mathbf{x}; t) = \sum_\sigma \rho_s^\sigma(\mathbf{x}; t)$ and the magnetization $m_s(\mathbf{x}; t) = \sum_\sigma \sigma \rho_s^\sigma(\mathbf{x}; t)$ of species s . These four functions (ρ_A , ρ_B , m_A , and m_B) determine completely the spin and species states at the position \mathbf{x} and the time t .

In appendix A, we derive the hydrodynamic equations for the reciprocal TSAIM. From the symmetries of the problem, we define the density $\rho = \sum_{s,\sigma} \rho_s^\sigma = \rho_A + \rho_B$, the species magnetization $m = \sum_{s,\sigma} s \rho_s^\sigma = \rho_A - \rho_B$, and the order parameters $v_s = \sum_{s,\sigma} \sigma \rho_s^\sigma = m_A + m_B$, and $v_a = \sum_{s,\sigma} s \sigma \rho_s^\sigma = m_A - m_B$. Since the classical mean-field approximation fails to exhibit phase-separated profiles, we follow the refined mean-field approximation used for the one-species AIM [13], which implies here to take m and v_a as independent Gaussian variables with a variance linear in the density ρ : $\sigma_m^2 = \alpha_m \rho$ and $\sigma_a^2 = \alpha_a \rho$, respectively. The hydrodynamic equations, averaged over the Gaussian variables, for the reciprocal TSAIM read

$$\partial_t \rho = D_{xx} \partial_x^2 \rho + D_{yy} \partial_y^2 \rho - v \partial_x v_s, \quad (9)$$

$$\partial_t m = D_{xx} \partial_x^2 m + D_{yy} \partial_y^2 m - v \partial_x v_a + 2\overline{\gamma_2} \left[\left(\rho - \frac{r_2}{2\beta_2} \right) \sinh \frac{2\beta_2 m}{\rho} - m \cosh \frac{2\beta_2 m}{\rho} \right], \quad (10)$$

$$\partial_t v_s = D_{xx} \partial_x^2 v_s + D_{yy} \partial_y^2 v_s - v \partial_x \rho + 2\overline{\gamma_1} \left[m \sinh \frac{2\beta_1 v_a}{\rho} - v_s \cosh \frac{2\beta_1 v_a}{\rho} \right], \quad (11)$$

$$\partial_t v_a = D_{xx} \partial_x^2 v_a + D_{yy} \partial_y^2 v_a - v \partial_x m + 2\overline{\gamma_1} \left[\left(\rho - \frac{r_1}{2\beta_1} \right) \sinh \frac{2\beta_1 v_a}{\rho} - v_a \cosh \frac{2\beta_1 v_a}{\rho} \right] + 2\overline{\gamma_2} \left[v_s \sinh \frac{2\beta_2 m}{\rho} - v_a \cosh \frac{2\beta_2 m}{\rho} \right], \quad (12)$$

with diffusion constants $D_{xx} = D + \theta v/2$, and $D_{yy} = D$, the self-propulsion velocity $v = 2D\varepsilon$, $\overline{\gamma_i} = \gamma_i \exp(r_i/2\rho)$, $r_1 = (2\beta_1)^2 \alpha_a$, and $r_2 = (2\beta_2)^2 \alpha_m$. Note that r_1 and r_2 are considered as two new parameters for the hydrodynamic theory and $r_1 = r_2 = 0$ within the classical mean-field approximation.

In appendix B, we derive the hydrodynamic equations for the non-reciprocal TSAIM. As for reciprocal interactions, we follow the refined mean-field approximation consisting here to take the magnetizations m_s as independent Gaussian variables with a variance linear in the density ρ : $\sigma_s^2 = \alpha_s \rho$. The hydrodynamic equations, averaged for the Gaussian variables, for the non-reciprocal TSAIM read:

$$\partial_t \rho_s = D_{xx} \partial_x^2 \rho_s + D_{yy} \partial_y^2 \rho_s - v \partial_x m_s, \quad (13)$$

$$\partial_t m_s = D_{xx} \partial_x^2 m_s + D_{yy} \partial_y^2 m_s - v \partial_x \rho_s + 2\overline{\gamma_s} \left[\left(\rho_s - \frac{r_1}{2\beta_1} \right) \sinh \frac{2\beta_1 \mu_s}{\rho} - m_s \cosh \frac{2\beta_1 \mu_s}{\rho} \right], \quad (14)$$

with diffusion constants $D_{xx} = D + \theta v/2$, and $D_{yy} = D$, the self-propulsion velocity $v = 2D\varepsilon$, $\mu_s = m_s + (J_{s,-s}/J_1)m_{-s}$, $\bar{\gamma}_s = \gamma_1 \exp[(r_1 + r_{s,-s})/2\rho]$, and $r_{ss'} = (2\beta J_{ss'})^2 \alpha_{s'} = (J_{ss'}/J_1)^2 r_1$, where r_1 can be considered as a new parameter in the context of the hydrodynamic theory.

We use explicit Euler Forward Time Centered Space (FTCS) [52] differencing scheme to numerically integrate the Eqs. (9)–(14). We solve these coupled partial differential equations on a one-dimensional ring of length L_x with periodic boundary conditions, for $D = 1$ and $\theta = 0$, i.e. $D_{xx} = D_{yy} = 1$ and $v = 2\varepsilon$. In our simulation, $L_x = 1024$ and the maximum simulation time is $t \simeq 10^5$. To maintain the numerical stability criteria, we set $\Delta x = 1$ and $\Delta t = 10^{-3}$ as the space and time discretizations, respectively. These discretization parameters satisfy the Courant-Friedrichs-Lewy (CFL) stability condition [53]. In our numerical implementation, the initial system is prepared as semi-ordered profiles with high-density regions of species A and B moving to the left or right (i.e. with positive or negative magnetization). The C++ codes used to compute the numerical solutions of Eqs. (9)–(14) are available in Ref. [51].

IV. RESULTS WITH RECIPROCAL INTERACTIONS AND NO SPECIES FLIP ($\gamma_2 = 0$)

In this section, we present the results of the reciprocal TSAIM without species flip ($\gamma_2 = 0$) for an equal population of the two species: $N_A = N_B = N/2$, i.e. $m_0 = 0$, which will stay constant over time. We aim to compare the results of this model, a model with discrete symmetry, with those obtained for the TSVM [33], a model characterized by continuous symmetry.

A. Steady-state profiles and phase diagrams

In this subsection, we present the results for a hopping rate, given by Eq. (1), with $\theta = 0$ and $D = 1$. Fig. 1 shows the steady-state density snapshots obtained from numerical simulations for increasing density starting from a semi-ordered PF configuration. At low densities ($\rho_0 < 3.98$), the particles of both species are disordered, forming a *gas* phase. At higher densities ($3.98 < \rho_0 < 6.82$), particles of both species exhibit flocking behavior in a moving transverse band, forming phase-separated density profiles, characterized by a band of each species moving together on a gaseous background composed of both A and B particles. These two bands are macrophase separated (i.e. only one band is observed in the steady state for each species, contrary to the TSVM), and define the *coexistence* region. The A- and B-band can either move in opposite directions, denoted as anti-parallel flocking (APF) [Fig. 1(a)], or in the same direction, denoted as parallel flocking (PF) [Fig. 1(b)]. In both the bands, A-particles are anti-aligned with B-particles

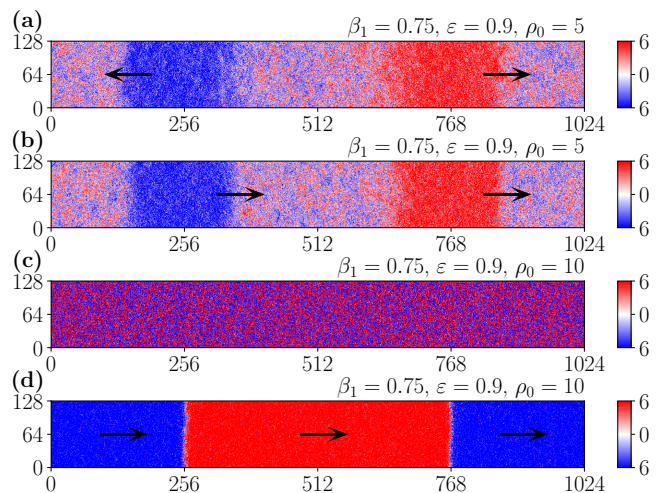


FIG. 1: (color online) Steady-state snapshots of the reciprocal TSAIM without species flip ($\gamma_2 = 0$) for $\beta_1 = 0.75$, $\varepsilon = 0.9$ and increasing density, in a 1024×128 domain, showing different states: coexistence (a) APF and (b) PF states for $\rho_0 = 5$, (c) liquid APF state, and (d) HDPF state for $\rho_0 = 10$. The densities of A and B species are represented with red and blue colors, respectively. At each site, the color corresponding to the species with the higher density is displayed. High-density bands move in the direction indicated by the arrows. A movie (movie 1) of the simulations is available in Ref. [54].

due to the antiferromagnetic interaction, yielding an opposite motion of B-particles inside the A-band, and vice versa. At even higher densities ($\rho_0 > 6.82$), the TSAIM exhibits a *liquid* state, though the morphology of this state is not unique. The homogeneous liquid phase can emerge where the densities of species A and species B are spatially uniformly distributed in an APF state, as shown in Fig. 1(c), similar to the liquid phase observed in the TSVM. Additionally, the system can also display a stable high-density PF (HDPF) state, characterized by two parallel flocking bands occupying half of the domain ($L_x/2 \times L_y$) [Fig. 1(d)]. Unlike in the TSAIM, this HDPF state is unstable in the TSVM [33], since the continuous symmetry implies giant number fluctuations [10], and fluctuations in the band orientation are also in favor of the APF state.

Fig. 2 shows instantaneous steady-state density profiles corresponding to Fig. 1. The phase-separated density profiles, shown in Fig. 2(a–b) and characterizing an APF and PF state, respectively, exhibit three distinct regions for each species: a maximum density in its own liquid band, an intermediate density in the gas phase outside both bands, and a minimum density in the liquid band of the other species. Due to the antiferromagnetic interaction between the two species, when a liquid band of species s moves to the right (left), with a positive (negative) magnetization, the particles of species $-s$ inside that band go to the left (right) with a negative (positive) magnetization. As the density increases, with an APF

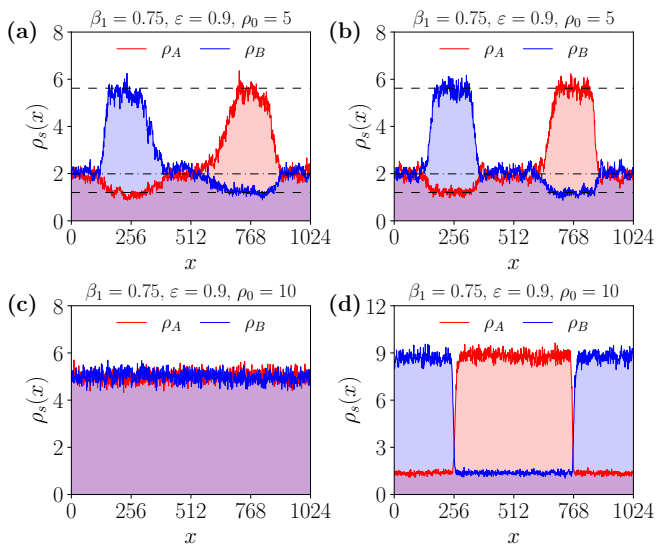


FIG. 2: (color online) Steady-state density profiles of the reciprocal TSAIM without species flip ($\gamma_2 = 0$), obtained from the density snapshots shown in Fig. 1 by integrating along the y -axis. The dashed and dash-dotted lines represent the main density values in the liquid and gas regions, respectively, as a guide to the eyes.

initial condition, both species exhibit homogeneous profiles around their average density, indicative of an APF state [Fig. 2(c)]. Starting from a PF initial condition, however, the system forms individual high-density bands for each species in the HDPF state, together spanning the x -axis [Fig. 2(d)]. In the HDPF state, no gas phase is present, leading to two distinct regions in the density profiles: a maximum density within the own band of each species and a minimum density within the band of the other species.

To understand the existence of this HDPF state, Fig. 3 shows the time evolution of the TSAIM starting from a disordered configuration, for which the steady state is in the HDPF state. We initially observe the nucleation of several flocks of species A and B moving either to the left or right [Figs. 3(a–c)]. As time progresses, these flocks grow, with pairs of parallel flocks of species A and B being favored [Fig. 3(d)]. This results in the formation of multiple PF bands arranged in layers along the y -axis [Fig. 3(e)], with alternating band motions to the left and right. At longer times, one of the layers becomes dominant, in this case moving to the right [Fig. 3(f)]. Conversely, in the TSVM [33], nucleating flocks are randomly oriented, not limited to anti-parallel or parallel flocking because of the continuous symmetry of spin orientation, and the growth of these nuclei does not favor the PF state over the APF state at large times.

Fig. 4(a) shows the probability p_{APF} of having an APF steady state, rather than a PF steady state, starting from a disordered initial configuration, as a function of the domain size L , calculated over 5000 different initial configurations

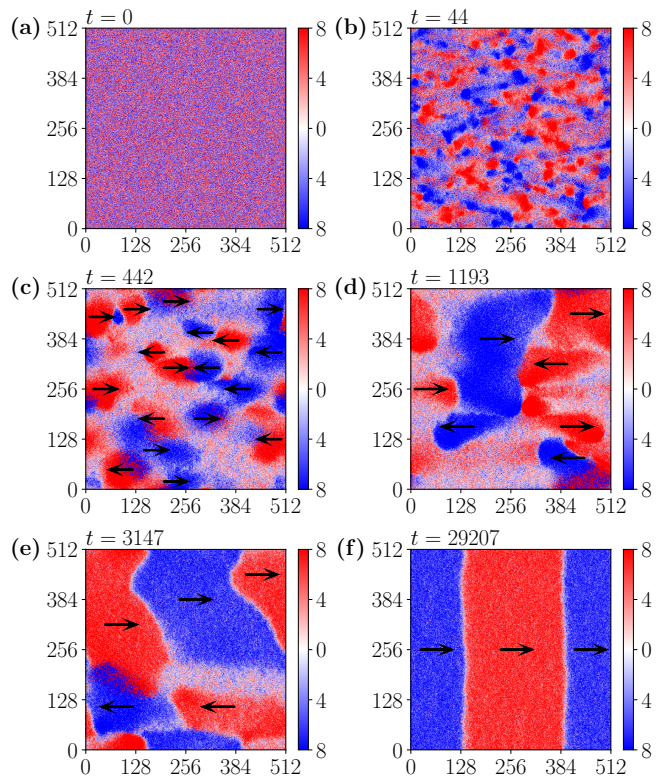


FIG. 3: (color online) Time evolution of the reciprocal TSAIM without species flip ($\gamma_2 = 0$) starting from a disordered initial configuration to an HDPF state for $\beta_1 = 0.75$, $\varepsilon = 0.9$, $\rho_0 = 8$ in a 512×512 domain (colormap as in Fig. 1).

urations and for several densities ρ_0 . A transition occurs between small system sizes, where the system exhibits an APF steady state for all realizations, and larger system sizes, where a PF steady state dominates. The probability p_{APF} becomes smaller than 1 (i.e., at least one configuration goes to a PF state) for $L > L_c$, with $L_c \sim 55$ for $\rho_0 \in \{8, 10\}$ and $L_c \sim 80$ for $\rho_0 = 5$, leading to HDPF and phase-separated PF steady states, respectively. This suggests that PF states are more *stable* than APF states in the hydrodynamic limit ($L \rightarrow \infty$) when starting from a disordered initial condition. It is important to note that, for semi-ordered initial conditions, the final TSAIM steady state is determined by the initial configuration, a PF (APF) initial condition always leads to a PF (APF) state. Indeed, we do not observe any fluctuation-induced stochastic switching between the APF and PF states in the TSAIM coexistence region, as seen in the TSVM [33], since the density fluctuations in the TSAIM are normal, similar to the one-species AIM [13].

We now discuss our results for non-motile limit ($\varepsilon = 0$) of the TSAIM, where the particles of both species only diffuse. A second-order phase transition similar to the one-species AIM is observed between a low-density, high-noise disordered state and a high-density, low-noise ordered state. Fig. 4(b) shows the mean value of the or-

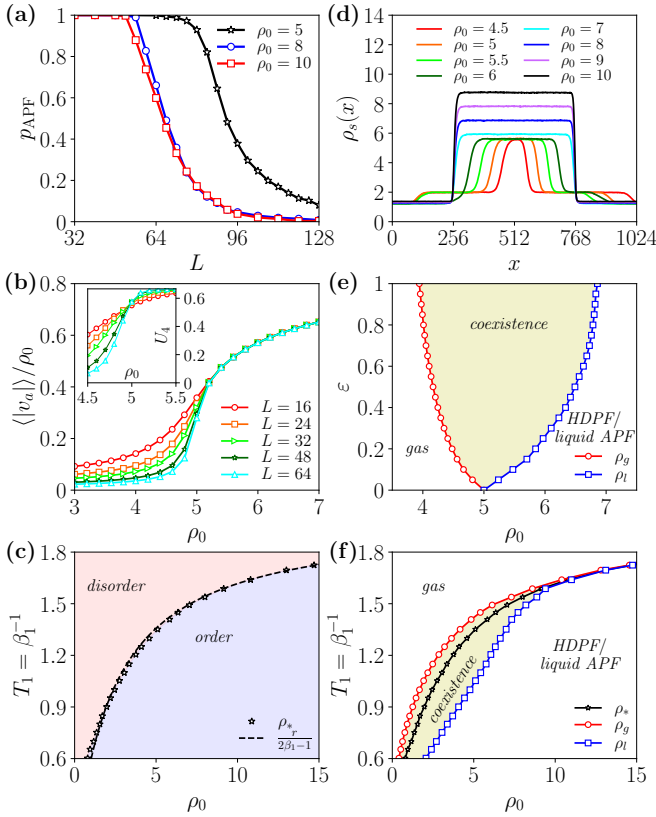


FIG. 4: (color online) Results for the reciprocal TSAIM without species flip ($\gamma_2 = 0$). (a) Probability for a steady state in the APF state as a function of the system size, starting from disordered initial configurations, calculated over 5000 ensembles for $\beta_1 = 0.75$, $\varepsilon = 0.9$ and several densities ρ_0 . (b) Mean value and Binder cumulant (inset) of the order parameter $|v_a|$ vs ρ_0 without activity ($\varepsilon = 0$) for $\beta_1 = 0.75$ and several system sizes. The transition occurs at density $\rho_* = 4.95$. (c) State diagram for $\varepsilon = 0$. $\rho_0 < \rho_*(T_1)$: disordered state (red), $\rho_0 > \rho_*(T_1)$: ordered state (blue). (d) Steady-state density profiles (PF state) for $\beta_1 = 0.75$ and $\varepsilon = 0.9$ in a 1024×128 domain, for various densities. The data are averaged over 1000 times. (e) Velocity-density state diagram for $\beta_1 = 0.75$. (f) Temperature-density state diagram for $\varepsilon = 0.9$.

der parameter $|v_a|$ as a function of the density ρ_0 for $\beta_1 = 0.75$ and several system sizes, which confirms the presence of this order-disorder phase transition. The density ρ_* at which the transition occurs can be determined by the Binder cumulant of the order parameter $U_4 = 1 - \langle v_a^4 \rangle / 3 \langle v_a^2 \rangle^2$ for several system sizes [inset of Fig. 4(b)]. The Binder cumulant is independent of the system size only at the transition point [55], which gives $\rho_* = 4.95$ for $\beta_1 = 0.75$. Repeating this procedure for several temperatures, we compute the temperature-density state diagram for $\varepsilon = 0$ as shown in Fig. 4(c). The transition line can be fitted by the expression $\rho_* = r / (2\beta_1 - 1)$, with $r \simeq 2.37$. This expression is compatible with our hydrodynamic theory and is analogous to the one-species

AIM.

We now move to the active case ($\varepsilon > 0$). Fig. 4(d) shows the steady-state density profiles $\rho_s(x)$ of a single species in the PF state for varying densities. These profiles are computed in a 1024×128 domain, integrated along the y -direction, and averaged both species and 1000 different times after the steady state is reached. For densities $\rho_0 < 6.82$, the profiles exhibit phase-separated PF bands similar to Fig. 1(b), where the density $\rho_s(x)$ takes three different values: maximum (larger than the gas density) in the liquid phase of species s with a positive magnetization m_s due to strong intra-species ferromagnetic interactions; intermediate in the gas phase with zero magnetization; and minimum (smaller than the gas density) in the liquid phase of the other species $-s$ with a negative magnetization m_s due to strong inter-species anti-ferromagnetic interactions. For densities $\rho_0 > 6.82$, the profiles correspond to an HDPF state as depicted in Fig. 1(d). From these density profiles, we determine the binodals: $\rho_g = 3.98$ and $\rho_l = 6.82$, as the minimum and maximum value of the total density $\rho = \rho_A + \rho_B$, defined such that for $\rho_0 < \rho_g$ the system is in the gas phase and $\rho_0 > \rho_l$ the system is in a liquid state (either liquid APF or HDPF state, depending on the initial condition). A stable HDPF state emerges solely due to the reciprocal anti-aligning interactions between the two species and therefore, is absent in the one-species flocking models [13–15]. To the best of our knowledge, this HDPF state has also not been observed in the TSVM [33] and any other multi-species active matter system.

We subsequently compute the binodals ρ_g and ρ_l for different temperatures and biases, and construct the velocity-density state diagram for $\beta_1 = 0.75$ [Fig. 4(e)] and the temperature-density state diagram for $\varepsilon = 0.9$ [Fig. 4(f)], both of which consist of the three typical regions of a flocking system: gas phase ($\rho_0 < \rho_g$), liquid state ($\rho_0 > \rho_l$), and the liquid-gas coexistence region ($\rho_g < \rho_0 < \rho_l$). The three line $\rho_g(T_1)$, $\rho_*(T_1)$ and $\rho_l(T_1)$ merge when $T_1 \rightarrow T_c = 2$.

B. Metastability and MIIP at small diffusivity

Next, we study the fate of the liquid states when the diffusivity is small compared to the velocity. To do this we choose the hopping rate W_{hop} (defined by Eq. (1)) with $\theta = 1$, i.e. $D + v$ in the favored direction and D in the three other directions. Figs. 5(a–b) depict the time evolution starting from the HDPF state with a diffusion constant $D = 0.05$ in a 2048×2048 domain. The bands initially move to the right ($\langle v_s \rangle > 0$). After 6000 Monte Carlo steps ($t = 698$), spontaneous nucleation of A and B droplets moving to the left appears within the high-density regions of both species [Fig. 5(a)]. This spontaneous nucleation destroys the long-range order characterized by bulk HDPF bands and observed for strong diffusion (W_{hop} with $\theta = 0$ and $D = 1$), and creates a new steady state formed of alternating A and B-rich

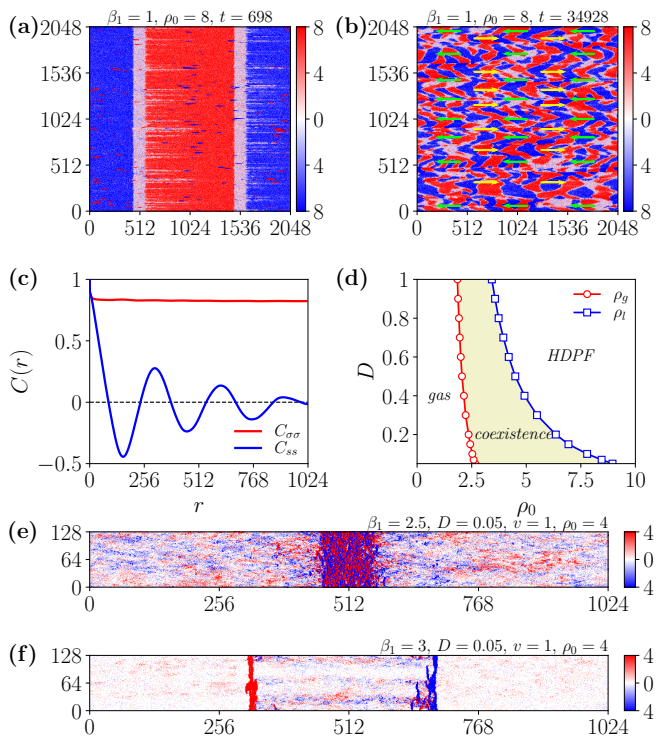


FIG. 5: (color online) Metastability and MIIP in the reciprocal TSAIM without species flip ($\gamma_2 = 0$). (a) Spontaneous nucleation of the HDPF state after 6000 MCS, for $\beta_1 = 1$, $D = 0.05$, $v = 1$ and $\rho_0 = 8$. (b) Steady-state after 300000 MCS (colormap as in Fig. 1). A movie (movie 2) of the simulation is available in Ref. [54]. (c) Spin-spin and species-species correlation functions along x : $C_{\sigma\sigma}(r) \sim \langle v_{s,i+r}v_{s,i} \rangle$ and $C_{ss}(r) \sim \langle m_i m_{i+r} \rangle$, respectively, for $\beta_1 = 1$, $D = 0.05$, $v = 1$, and $\rho_0 = 12$, and calculated in a 2048×128 domain. (d) Diffusion-density state diagram for $\beta_1 = 1$ and $v = 1$. (e-f) Motility-induced pinning for $D = 0.05$, $v = 1$, $\rho_0 = 4$, and several temperatures: (e) $\beta_1 = 2.5$ and (f) $\beta_1 = 3$ (colormap as in Fig. 1). A movie (movie 4) of the simulations is available in Ref. [54].

PF clusters arranged in stripes along the y -axis, going successively to the right and the left [Fig. 5(b)]. This morphology exhibits short-range order in species but displays strong spin correlations within each stripe, unlike the one-species AIM where clusters exhibit short-range order in spin [20]. The system is in the coexistence region, and further increasing the density does not alter the morphology but instead leads to a transition to an HDPF state. Similarly, starting from a liquid APF state, spontaneous nucleation of A and B droplets appears, and the system relaxes to the same steady state as depicted in Fig. 5(b). A movie (movie 3) depicting the fate of the liquid APF state is available in Ref. [54].

We now analyze this new steady-state formed by the spontaneous nucleation of droplets in the HDPF state and estimate the typical sizes of the steady-state A and B clusters. Fig. 5(c) shows the spin-spin and the species-species correlation functions, defined as $C_{\sigma\sigma}(r) \sim$

$\langle v_{s,i+r}v_{s,i} \rangle$ and $C_{ss}(r) \sim \langle m_{i+r}m_i \rangle$, respectively, where $\langle \cdot \rangle$ represents spatial, temporal and ensemble averaging, and calculated in a 2048×128 domain. The spin-spin correlation function $C_{\sigma\sigma}(r)$ does not decay to zero along the x direction, demonstrating the long-range order in the spin of the new steady state. The species-species correlation function $C_{ss}(r)$ decays to zero along the x direction, and shows the structure of PF clusters in a stripe such that $C_{ss}(r) \sim \cos(\lambda_x r) \exp(-r/\xi_x)$ with a correlation length $\xi_x \simeq 128$. These pronounced oscillations of $C_{ss}(r)$, although damped, are the signature of a phase-segregated repeated pattern often observed in binary fluid [56] and are also characteristic of antiferromagnetic interactions. Akin to the one-species AIM [20], the species-species correlation function exhibits an exponential decay along the y -axis with a correlation length $\xi_y \simeq 24$. These correlation functions demonstrate the short-range order in species of the new steady state and give a characteristic size to the constitutive clusters via the correlation lengths ξ_x and ξ_y , independent of the system size.

Fig. 5(d) shows the diffusion-density state diagram for $v = 1$ and $\beta_1 = 1$, computed in the same way as the state diagrams in Figs. 4(e-f) but for the hopping rate W_{hop} with $\theta = 1$. The gas and liquid binodals ρ_g and ρ_l decrease with D , meaning one enters the *coexistence* region when decreasing the diffusion constant at fixed density. For a diffusion constant $D \lesssim 0.15$, the bulk HDPF bands are no longer stable and the system exhibits a steady-state morphology as depicted in Fig. 5(b).

Similarly to the one-species AIM [20], the TSAIM exhibits motility-induced interface pinning (MIIP) at large values of β_1 (low temperatures), enhanced in the presence of small diffusion. The mechanism responsible for influencing the system's dynamics and the emergence of the MIIP transition can be attributed to the development of distinct timescales: a particle hops at a rate of $4D + v$, slow compared to the flipping which scales as $\exp(2\beta_1)$ [20]. The MIIP state is characterized by a pinned or jammed interface, with $\sigma = +1$ particles on the left and $\sigma = -1$ particles on the right of the interface. At zero temperature, this structure is stable since a $\sigma = +1$ particle will move to the right and reach a site populated with only $\sigma = -1$ particles and then instantaneously flip to $\sigma = -1$, and returns, creating a back-and-forth oscillation at the interface. Figs. 5(e-f) illustrate the MIIP state for $D = 0.05$ and increasing values of β_1 . For $\beta_1 = 2.5$, the MIIP state consists of pinned interfaces formed by particles of both species, with many active particles moving outside of this structure and not contributing to the formation of the pinned interfaces [Fig. 5(e)]. As we increase the inverse temperature to $\beta_1 = 3$, the interface pinning strengthens, resulting in the MIIP state being defined by two distinct, high-density pinned interfaces of each species, with a greater number of particles actively contributing to the formation of these interfaces [Fig. 5(f)]. The MIIP states, shown in Figs. 5(e-f), are independent of the initial condition (disordered, liquid

APF, or HDPF state), however, with an HDPF or a liquid APF initial condition, these MIIP states can only be formed after counter-propagating droplets have spontaneously nucleated to create the pinned interface, which is enhanced when D is small compared to v .

C. Hydrodynamic theory

We now present the results obtained from the hydrodynamic theory derived in Sec. III, via the solution of the Eqs. (9)-(12) for $\gamma_2 = 0$. The non-motile case, for which $\varepsilon = 0$ (i.e. $v = 0$), exhibits only homogeneous stationary solutions: $\rho(x) = \rho_0$, $m(x) = m_0$, and the order parameters following the equations:

$$v_s = m_0 \tanh \frac{2\beta_1 v_a}{\rho_0}, \quad (15)$$

$$v_a = \left(\rho_0 - \frac{r_1}{2\beta_1} \right) \tanh \frac{2\beta_1 v_a}{\rho_0}. \quad (16)$$

Considering the same average density for each species ($\langle \rho_s(x) \rangle = \rho_0/2$, where $\langle \cdot \rangle$ denotes the spatial averaging here) at initial condition, i.e. $\langle m(x) \rangle = m_0 = 0$, we get $v_s = 0$. From Eq. (16), we get a second-order phase transition between a disordered homogeneous solution ($v_a = 0$) and an ordered homogeneous solution ($|v_a| > 0$). The transition occurs when $2\beta_1 - r_1/\rho_0$ is larger than 1, i.e. for a density larger than $\rho_* = r_1/(2\beta_1 - 1)$ and for a temperature $T_1 < T_c = 2$. This expression is compatible with the transition line obtained from the simulations of the microscopic model and shown in Fig. 4(c).

Phase-separated density profiles can be observed for a positive velocity ($\varepsilon > 0$). Figs. 6(a) and 6(b) show steady-state density profiles $\rho_s(x)$ as APF and PF states, respectively. Fig. 6(c) shows steady-state density profiles ρ_s in the PF state for increasing density. For densities $\rho_0 < 1.31$, the profiles exhibit phase-separated PF bands similar to Fig. 6(b), for a right-moving band. The density $\rho_s(x)$ takes three different values: in the liquid phase of species s ($m_s > 0$), in the gas phase ($m_s = 0$), and in the liquid phase of the other species $-s$ ($m_s < 0$). For densities $\rho_0 > 1.31$, the HDPF state is observed and explained with Eqs. (9)-(12) as follows: in the A-band, the density is homogeneous such that $\rho_A > \rho_B$ and the order parameter v_a obeys the ordered homogeneous solution. Then v_s satisfies Eq. (15) where m_0 is replaced by $\rho_A - \rho_B$, which determines the magnetization of species A: $m_A = (v_s + v_a)/2$ and species B: $m_B = (v_s - v_a)/2$, such that m_A and m_B have different signs. We determine the binodals from these density profiles: $\rho_g = 0.986$ and $\rho_l = 1.31$. Computing the binodals for several velocities and temperatures, we construct the velocity-density state diagram for $\beta_1 = 0.75$ [Fig. 6(d)] and the temperature-density state diagram for $\varepsilon = 0.9$ [Fig. 6(e)]. We recover the three typical regions of a flocking system: gas phase ($\rho_0 < \rho_g$), liquid state ($\rho_0 > \rho_l$), constituted with the liquid APF state and the HDPF state, and the liquid-gas

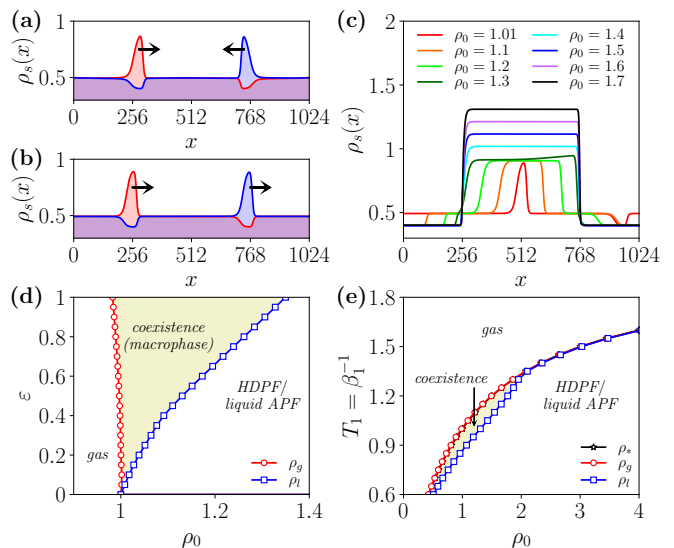


FIG. 6: (color online) Hydrodynamic theory of reciprocal TSAIM without species flip ($\gamma_2 = 0$). (a–b) Steady-state density profile for $\rho_0 = 1.01$ showing (a) an APF state and (b) a PF state. (c) Steady-state density profile for increasing densities in the PF state. Parameters: $\beta_1 = 1$, $\varepsilon = 0.9$, and $L_x = 1024$. (d) Velocity-density state diagram for $\beta_1 = 1$. (e) Temperature-density state diagram for $\varepsilon = 0.9$.

coexistence region ($\rho_g < \rho_0 < \rho_l$).

V. RESULTS WITH RECIPROCAL INTERACTIONS AND SPECIES FLIP ($\gamma_2 = 0.5$)

In this section, we present the results of the reciprocal TSAIM with species flip, with species interaction given by Eq. (7) with $\gamma_2 = 0.5$, for which the number of particles of each species, N_A and N_B , is not conserved. Depending on the initial species magnetization $m_0 = (N_A - N_B)/L_x L_y$, the TSAIM dynamics drive the system into different steady states.

A. Steady-state profiles and phase diagrams

In this subsection, we present the results for a hopping rate, given by Eq. (1), with $\theta = 0$ and $D = 1$. Figs. 7(a–d) show the steady-state density profiles obtained from the simulation of the microscopic model, for $\beta_1 = 0.75$ and $\beta_2 = 1.5$ ($\beta_2 > \beta_1$), starting from a semi-ordered configuration. As shown, the steady state strongly depends on the initial population of each species. At very low densities ($\rho_0 < 0.8$), the steady state is disordered in both spin and species, forming a *paramagnetic gas* phase (see appendix C).

Starting from a configuration with all particles of species A ($m_0 = \rho_0$), for $\rho_0 > 0.8$, the system exhibits a liquid-gas phase transition of species A similar

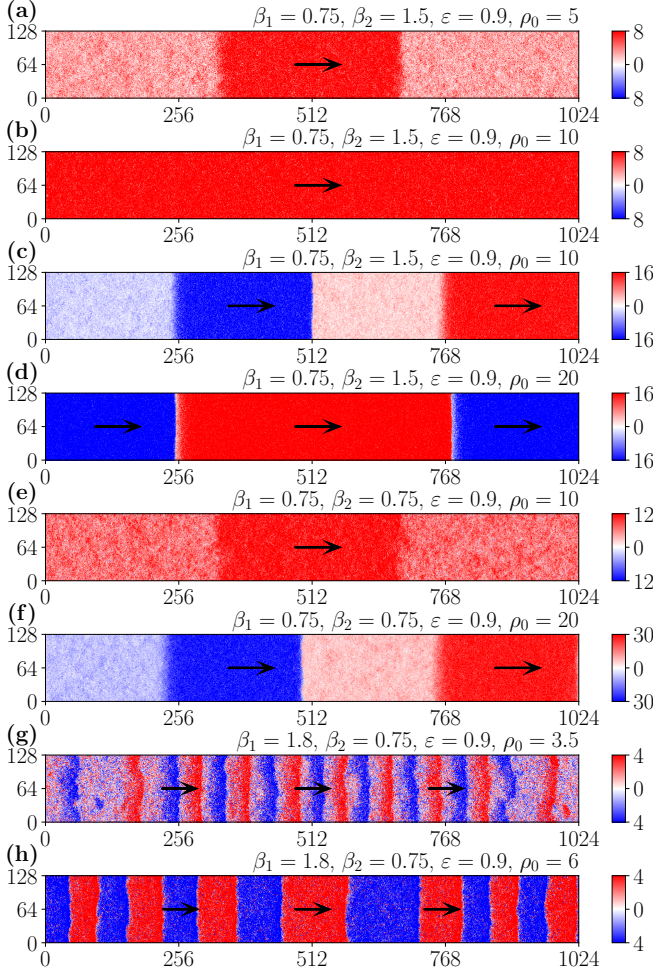


FIG. 7: (color online) Steady-state density snapshots of the reciprocal TSAIM with species flip ($\gamma_2 = 0.5$) for $\varepsilon = 0.9$, in a 1024×128 domain. (a–d) Snapshots for $\beta_1 = 0.75$ and $\beta_2 = 1.5$: (a) one-species coexistence state ($\rho_0 = 5$), (b) one-species liquid phase ($\rho_0 = 10$), (c) two-species coexistence PF state ($\rho_0 = 10$), and (d) HDPF state ($\rho_0 = 20$). (e–f) Snapshots for $\beta_1 = \beta_2 = 0.75$: (e) one-species coexistence state ($\rho_0 = 10$), and (f) two-species coexistence PF state ($\rho_0 = 20$). (g–h) Snapshots for $\beta_1 = 1.8$ and $\beta_2 = 0.75$: (g) two-species coexistence PF state ($\rho_0 = 3.5$), and (h) HDPF state ($\rho_0 = 6$) exhibiting microphase separation (colormap as in Fig. 1). A movie (movie 5) of the simulations is available in Ref. [54].

to the one-species AIM, where the particles in species B remain disordered for all densities. At low densities ($0.8 < \rho_0 < 2.86$), the particles of species A are disordered in spin, but ordered in species, forming a *ferromagnetic gas* phase of species A (see appendix C). At larger densities ($2.86 < \rho_0 < 9.13$), the particles in species A start flocking in a transverse band, showing macrophase-separated density profiles, which characterizes the *coexistence* region [Fig. 7(a)]. At even higher densities ($\rho_0 > 9.13$), the band of species A spans the whole domain, forming a *liquid* phase of species A [Fig. 7(b)].

But, if we start with an initial configuration where both species are equally populated ($m_0 = 0$), the scenario differs from the one-species AIM and the reciprocal TSAIM without species flip studied in Sec. IV. At low densities ($0.8 < \rho_0 < 2.95$), particles of both species are disordered in spin, but ordered in species, which also leads to a *ferromagnetic gas* phase of both species (see appendix C). At higher densities ($2.95 < \rho_0 < 17.0$), both species exhibit transverse band motion, forming macrophase-separated density profiles, with a band of each species followed by its gas phase [Fig. 7(c)], characterizing the PF *coexistence* region. At even higher densities ($\rho_0 > 17.0$), the two bands span the whole domain, with no gas phase present, forming a HDPF state [Fig. 7(d)], as observed for the reciprocal TSAIM without species flip, in Sec. IV. However, the liquid APF state is not observed in the presence of species flip. Furthermore, Figs. 7(b) and 7(c) are obtained for the same parameters, but different initial configurations, leading to two different steady states: a one-species liquid phase and a two-species phase-separated profile, respectively.

Figs. 7(e–f) show the steady-state density profiles, for $\beta_1 = \beta_2 = 0.75$, starting from a semi-ordered configuration. For this value of β_2 , the steady states are similar to the ones observed for $\beta_2 > 1.5$: a paramagnetic gas phase (for $\rho_0 < 3.95$), a ferromagnetic gas phase (for $3.95 < \rho_0 < 8.0$), a one-species macrophase-separated profile (for $8.0 < \rho_0 < 14.0$) as shown in Fig. 7(e), a one-species liquid phase (for $\rho_0 > 14.0$), a two-species macrophase-separated profile (for $8.0 < \rho_0 < 31.0$) as shown in Fig. 7(d), and an HDPF state (for $\rho_0 > 31.0$), depending on the initial condition. As shown in Fig. 8, the only difference between $\beta_2 = 1.5$ and $\beta_2 = 0.75$ lies in the proportion of A and B-particles in each site: for $\beta_2 = 1.5$, most of the sites of the steady states shown in Figs. 7(a–d) are occupied by a unique species (either A or B depending on the position), while for $\beta_2 = 0.75$, all the sites of the steady states shown in Figs. 7(e–f) are occupied by the two species (but one has a higher population, depending on the position). This behavior is due to the increase of species magnetization m , i.e. a stronger order in species, when β_2 increases.

Figs. 7(g–h) show the steady-state density profiles, for $\beta_1 = 1.8$ and $\beta_2 = 0.75$ ($\beta_1 > \beta_2$), starting from a disordered configuration. Here, the steady state does not depend on the initial population of each species. At low density ($\rho_0 < 2.11$), the particles are in a disordered state for both spin and species, forming the *paramagnetic gas* phase. At higher densities ($2.11 < \rho_0 < 4.67$), both species exhibit transverse band motion, forming *microphase-separated* density profiles, with several PF bands of both species [Fig. 7(g)]. These microphase-separated density profiles have not been observed in the one-species AIM [13] or TSAIM without species flip (Sec. IV), which only exhibit macrophase-separated profiles. At even higher densities ($\rho_0 > 4.67$), these microphase-separated bands span the whole domain forming an HDPF state [Fig. 7(h)], similar to

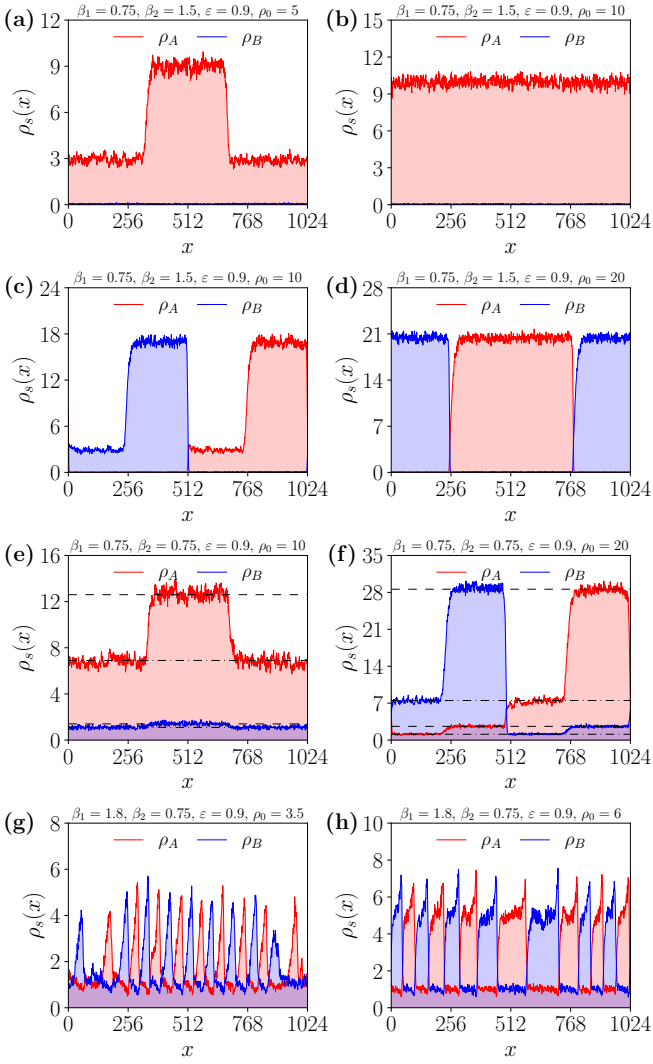


FIG. 8: (color online) Steady-state density profiles of the reciprocal TSAIM with species flip ($\gamma_2 = 0.5$), obtained from the density snapshots shown in Fig. 7 by integrating along the y -axis. The dashed and dash-dotted lines represent the main density values in the liquid and gas regions, respectively, as a guide to the eyes.

Fig. 7(d) where only two bands are present. This steady state is obtained from a quench and has the signature of a dynamical process with microphase-separated profiles at intermediate times, during the formation of flocks. A steady state with any even number of bands would remain stable within this parameter set. Additional density profiles are shown in Fig. 24 and discussed in appendix D. The origin of these microphase-separated profiles is discussed in the context of Fig. 11.

Fig. 8 shows the instantaneous steady-state density profiles corresponding to Fig. 7. For $\beta_1 = 0.75$ and $\beta_2 = 1.5$ ($\beta_2 > \beta_1$), starting from all particles of species A ($m_0 = \rho_0$), the density profiles are similar to the one-species AIM: homogeneous gas profiles at low densi-

ties, macrophase-separated density profile at intermediate densities [Fig. 8(a)], and homogeneous liquid density profiles of species A at high densities [Fig. 8(b)]. Starting from an equal population of both species ($m_0 = 0$), the macrophase-separated bands of each species are characterized by a PF state, where the high-density liquid band of each species is followed by its own low-density gas phase [Fig. 8(c)]. At higher ρ_0 , the low-density gas phases vanish and the high-density liquid bands span the x -axis forming an HDPF state [Fig. 8(d)]. For this value of β_2 , only one of the two species has a positive value (up to fluctuations) at a given position x . For $\beta_1 = \beta_2 = 0.75$, starting from all particles of species A, the macrophase-separated density profile exhibits a gaseous background of species B with a slightly higher density inside the liquid band of species A [Fig. 8(e)]. Starting from an equal population of both species, the macrophase-separated density profiles (within a PF state) exhibit four distinct regions for each species: a maximum density in its own liquid band, a high intermediate density in its own gas phase (located behind its liquid band), a low intermediate density in the liquid band of the other species, and a minimum density in the gas phase of the other species (located behind the liquid band of this species). Contrary to the reciprocal TSAIM without species flip (see Sec. IV), the species-species interaction dominates the antiferromagnetic spin-spin interaction meaning that the magnetization of the species s is non-zero only in the liquid band of species s , and the density ratio between both species depends only on the species magnetization m , such that $\rho_A/\rho_B = (1 + M)/(1 - M)$, where $M = m/\rho = (\rho_A - \rho_B)/(\rho_A + \rho_B)$ has a constant modulus over x ($M \simeq \pm 0.8$ for $\beta_2 = 0.75$), leading to the four values taken by ρ_s in gas and liquid regions. For $\beta_1 = 1.8$ and $\beta_2 = 0.75$ ($\beta_1 > \beta_2$), multiple alternating high-density bands of species A and B emerge in a PF state on a low-density gas background [Fig. 8(g)], and as the density increases, the average width and height of these bands expand and span the whole region [Fig. 8(h)].

Fig. 9 shows the time evolution of the TSAIM with species flip starting from a disordered configuration (both in spin and species), for which the steady-state is in one of the liquid states (for either $m_0 = 0$ or $m_0 = \rho_0$). Since β_2 and ρ_0 are large, at short times, we observe a species ordering for all the sites (decided by the sign of m_i), before the nucleation of several flocks of species A and B moving either to the left or right [Figs. 9(a-c)]. These flocks grow with time, with a gas phase of the same species following each polar flock [Fig. 9(d)]. This results in the formation of one-species flocking arranged in layers along the y -axis [Fig. 9(e)], with alternating species (A and B) but random flocking directions. At longer times, one of the layers becomes dominant, in this case, a liquid of species A moving to the right [Fig. 9(f)]. The HDPF state can also be observed as a steady state, but less probable than the one-species liquid phase.

We now discuss the non-motile case ($\varepsilon = 0$), where the particles of both species only diffuse, in addition to the

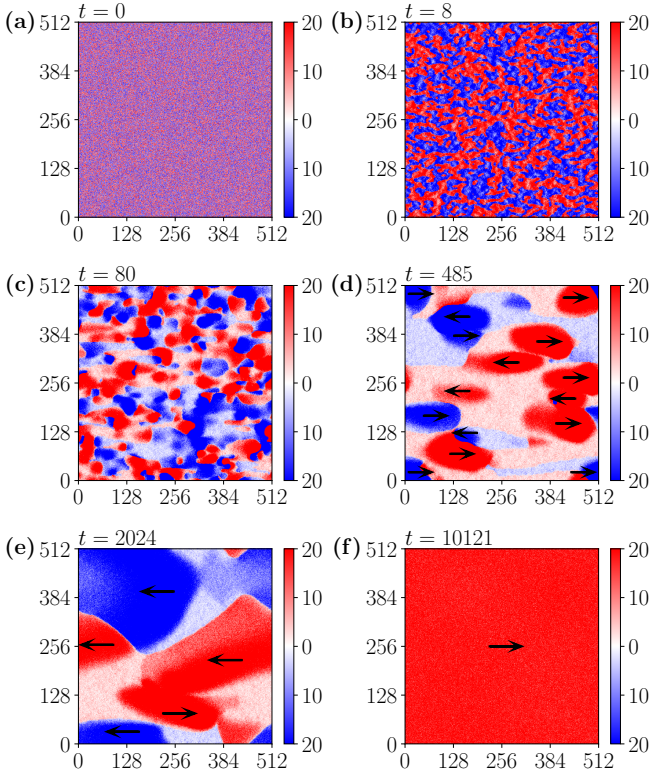


FIG. 9: (color online) Time evolution of the reciprocal TSAIM with species flip ($\gamma_2 = 0.5$) starting from a disordered initial configuration to a one-species liquid phase for $\beta_1 = 0.75$, $\beta_2 = 1.5$, $\varepsilon = 0.9$, $\rho_0 = 20$ in a 512×512 domain (colormap as in Fig. 1).

spin and species interactions. A second-order phase transition occurs for both m and v_a order parameters between a disordered state at low density and high noise, and an ordered state at high density and low noise. Figs. 10(a–b) show the mean value of the order parameters $\langle m \rangle$ and $\langle v_a \rangle$ as a function of the density ρ_0 for $\beta_1 = \beta_2 = 0.75$ and several system sizes, which confirms the presence of an order-disorder phase transition for both m and v_a . The densities ρ_2^* and ρ_1^* at which both the phase transitions occur can be derived from the Binder cumulant of the two order parameters: $U_4^m = 1 - \langle m^4 \rangle / 3\langle m^2 \rangle^2$ and $U_4 = 1 - \langle v_a^4 \rangle / 3\langle v_a^2 \rangle^2$, respectively [insets of Figs. 10(a–b)]. The Binder cumulant is independent of the system size only at the transition point [55], which gives $\rho_2^* = 3.95$ for the species phase transition (crossing of U_4^m), and $\rho_1^* = 11.25$ for the spin-orientation phase transition (crossing of U_4) for $\beta_1 = \beta_2 = 0.75$. Repeating this procedure for several β_1 and β_2 , we compute the temperature-density state diagrams shown in Figs. 10(c–d). From the flipping rates, given by Eqs. (2) and (7), the density $\rho_2^* \equiv \rho_2^*(T_2)$ will only depend on T_2 where the density $\rho_1^* \equiv \rho_1^*(T_1, T_2)$ will depend on both the temperatures T_1 and T_2 . The transition line can be fitted by the expression $\rho_2^*(T_2) = r_2 / (2\beta_2 - 1)$, with $r_2 \simeq 1.85$.

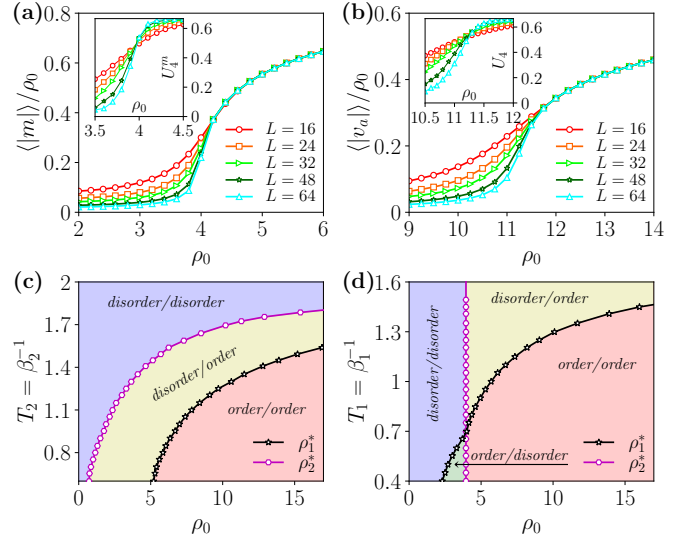


FIG. 10: (color online) Order parameter and state diagrams of the reciprocal TSAIM with species flip ($\gamma_2 = 0.5$) for $\varepsilon = 0$. (a–b) Mean value and Binder cumulant (insets) of the order parameters $|m|$ and $|v_a|$ vs ρ_0 for $\beta_1 = 0.75$, $\beta_2 = 0.75$, and several system sizes. The transitions occur at densities $\rho_2^* = 3.95$ and $\rho_1^* = 11.25$. (c) Temperature T_2 -density state diagram for $\beta_1 = 0.75$, and (d) temperature T_1 -density state diagram for $\beta_2 = 0.75$. $\rho_0 < \min(\rho_1^*, \rho_2^*)$: spin disordered/species disordered state with $\langle m \rangle = 0$ and $\langle v_a \rangle = 0$ (blue), $\rho_2^* < \rho_0 < \rho_1^*$: spin disordered/species ordered state with $\langle m \rangle > 0$ and $\langle v_a \rangle = 0$ (yellow), $\rho_1^* < \rho_0 < \rho_2^*$: spin ordered/species disordered state with $\langle m \rangle = 0$ and $\langle v_a \rangle > 0$ (green), and $\rho_0 > \max(\rho_1^*, \rho_2^*)$: spin ordered/species ordered state with $\langle m \rangle > 0$ and $\langle v_a \rangle > 0$ (red).

This expression is compatible with hydrodynamic theory and analogous to the one-species AIM. The lines ρ_1^* and ρ_2^* partition the state diagram into four regions in which spin and species can be either disordered or ordered. These four non-motile states are similar to those reported for the AT model [50], for the order parameters $\langle v_s \rangle \sim \langle \sigma \rangle$, $\langle m \rangle \sim \langle s \rangle$, and $\langle v_a \rangle \sim \langle \sigma s \rangle$: (i) a paramagnetic phase where $\langle \sigma \rangle = \langle s \rangle = \langle \sigma s \rangle = 0$ [disorder/disorder in Fig. 10 (blue)], (ii) a symmetric Baxter phase where $\langle \sigma \rangle = \pm \langle s \rangle \neq 0$ and $\langle \sigma s \rangle \neq 0$ [order/order in Fig. 10 (red)], (iii) a $\langle \sigma s \rangle$ phase where $\langle \sigma s \rangle \neq 0$ and $\langle \sigma \rangle = \langle s \rangle = 0$ [order/disorder in Fig. 10 (green)], and (iv) a $\langle s \rangle$ phase where $\langle s \rangle \neq 0$ and $\langle \sigma \rangle = \langle \sigma s \rangle = 0$ [disorder/order in Fig. 10 (yellow)].

We now move to the active case ($\varepsilon > 0$). Figs. 11(a–b) shows the steady-state density profiles $\rho_s(x)$ in the PF state obtained from numerical simulations for increasing densities. These profiles are computed in a 1024×128 domain, integrated along the y -direction, and averaged over both species and 1000 different times after the steady state is reached, following the two different initial populations of each species: $m_0 = \rho_0$ in Fig. 11(a) and $m_0 = 0$ in Fig. 11(b). Starting with $m_0 = \rho_0$, the density profiles are analogous to the one-species AIM [13]. Starting

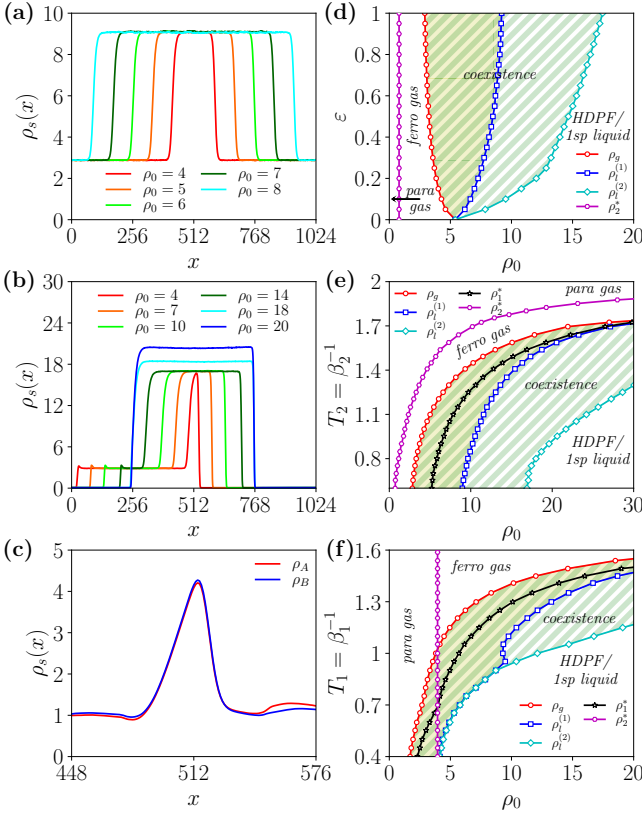


FIG. 11: (color online) Results of the reciprocal TSAIM with species flip ($\gamma_2 = 0.5$). (a–b) Steady-state density profiles (PF state) for $\beta_1 = 0.75$, $\beta_2 = 1.5$, and $\varepsilon = 0.9$ in a 1024×128 domain, for various densities. The initial configuration is taken with (a) $m_0 = \rho_0$ or (b) $m_0 = 0$. (c) Steady-state density profile of a single band for $\beta_1 = 1.8$, $\beta_2 = 0.75$, and $\varepsilon = 0.9$ in a 1024×128 domain, corresponding to the microphase separated snapshot shown in Fig. 7(g). The data are averaged over 1000 times. (d) Velocity-density state diagram for $\beta_1 = 0.75$ and $\beta_2 = 0.75$. (e) Temperature T_2 -density state diagram for $\beta_1 = 0.75$ and $\varepsilon = 0.9$. (f) Temperature T_1 -density state diagram for $\beta_2 = 0.75$ and $\varepsilon = 0.9$.

from $m_0 = 0$ and for densities $\rho_0 < 17.0$, the profiles exhibit phase-separated PF bands similar to Fig. 7(c), where the density $\rho_s(x)$ assumes four distinct values corresponding to the liquid phase and the ferromagnetic gas phase, dominated either by species s or by the opposing species $-s$. Starting from $m_0 = 0$ and for densities $\rho_0 > 17.0$, the profiles correspond to an HDPF state as depicted in Fig. 7(d). We determine from these density profiles the value of the binodals for both initial conditions: $\rho_g^{(1)} = 2.86$ and $\rho_l^{(1)} = 9.13$, as the minimum and maximum value of ρ_A when only species A is present, and $\rho_g^{(2)} = 2.95$ and $\rho_l^{(2)} = 17.0$, as the minimum and maximum value of the total density $\rho = \rho_A + \rho_B$ when both species are present. As we can see $\rho_g^{(1)} \simeq \rho_g^{(2)} \equiv \rho_g$ since the system is in the same gas phase for both scenarios when $\rho_0 < \rho_g$. However, we can see that $\rho_l^{(1)} < \rho_l^{(2)}$

since the two liquid states are completely different and the antiferromagnetic interaction between the two species makes the value of the binodal higher.

Fig. 11(c) shows the steady-state density profile $\rho_s(x)$ of a single band obtained from numerical simulations, corresponding to the microphase separated snapshot shown in Fig. 7(g). This profile is computed in a 1024×128 domain by first performing a running average on the time-dependent density profiles, integrated along the y -direction, to merge the multiple bands corresponding to the microphase separation. The resulting profiles are then averaged over 1000 times, and both species. We determine the gas and liquid binodals: $\rho_g = 2.11$ and $\rho_l^{(2)} = 4.67$, respectively, from this density profile.

We compute analogously the binodals ρ_g , $\rho_l^{(1)}$, and $\rho_l^{(2)}$ for different temperatures T_1 , T_2 , and biases ε , and construct the velocity-density state diagram for $\beta_1 = 0.75$ and $\beta_2 = 1.5$ [Fig. 11(d)], the temperature T_2 -density state diagram for $\beta_1 = 0.75$ and $\varepsilon = 0.9$ [Fig. 11(e)], and the temperature T_1 -density state diagram for $\beta_2 = 0.75$ and $\varepsilon = 0.9$ [Fig. 11(f)], which consists of four regions: paramagnetic gas phase ($\rho_0 < \rho_2^*$), ferromagnetic gas phase ($\rho_2^* < \rho_0 < \rho_g$), coexistence region ($\rho_g < \rho_0 < \rho_l$), and liquid state ($\rho_0 > \rho_l$), where ρ_l can either be $\rho_l^{(1)}$ or $\rho_l^{(2)}$, depending on the initial configuration. This liquid state is characterized by a one-species liquid phase (*1sp liquid*) for $\rho_0 > \rho_l^{(1)}$, as shown in Fig. 7(b), or by an HDPF state for $\rho_0 > \rho_l^{(2)}$, as depicted in Fig. 7(d). The coexistence region can be further decomposed into three subregions: (i) $\rho_2^* < \rho_g < \rho_1^*$ where a ferromagnetic gas phase coexists with a macrophase-separated liquid band [Fig. 7(a)], (ii) $\rho_g < \rho_2^* < \rho_1^*$ where a paramagnetic gas phase coexists with a macrophase-separated liquid band [Fig. 7(c)], and (iii) $\rho_g < \rho_1^* < \rho_2^*$ where a paramagnetic gas phase coexists with microphase-separated liquid bands emerging from the frustration of the spin ordered but species disordered state [Fig. 7(g)]. Note that the liquid binodals, $\rho_l^{(1)}$ and $\rho_l^{(2)}$, will always be larger than ρ_g , ρ_1^* , and ρ_2^* since flocking is possible only when both species and spin are ordered.

B. Metastability and MIIP with species flip

Similarly to the TSAIM without species flip (see Sec. IV) and the one-species AIM [19, 20], the liquid states are not stable when the diffusion is small compared to the velocity, and we consider the hopping rate W_{hop} (defined by Eq. (1)) with $\theta = 1$, i.e. $D + v$ in the favored direction and D in the three other directions. Figs. 12(a–b) depict the time evolution starting from the HDPF state with a diffusion constant $D = 0.05$ in a 2048×2048 domain. The band movement initially goes to the right ($\langle v_s \rangle > 0$). After 13000 Monte Carlo steps ($t = 697$), spontaneous nucleation of A and B droplets moving to the left appears within the high-density regions of both

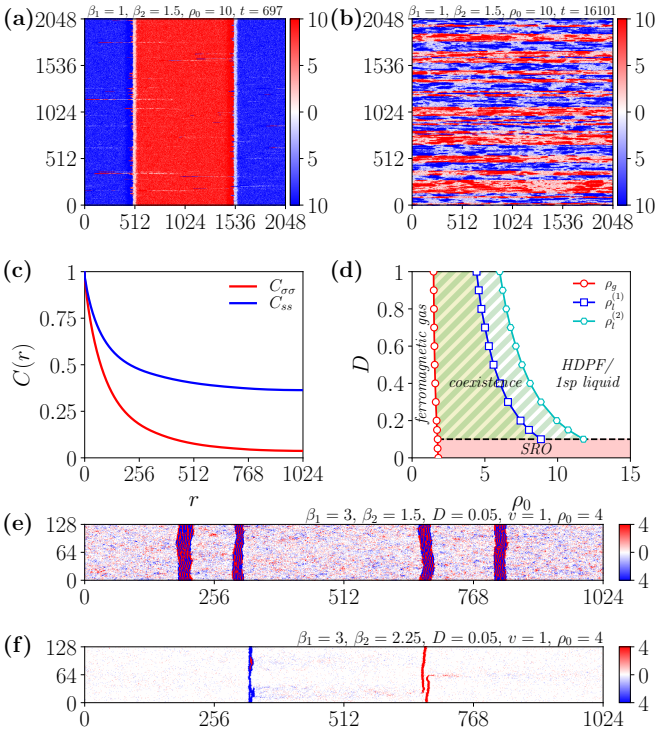


FIG. 12: (color online) Metastability and MIIP in the reciprocal TSAIM with species flip ($\gamma_2 = 0.5$). (a) Spontaneous nucleation of the HDPF state after 13000 MCS, for $\beta_1 = 1, \beta_2 = 1.5, D = 0.05, v = 1$, and $\rho_0 = 10$. (b) Steady state after 300000 MCS (colormap as in Fig. 1). A movie (movie 6) of the simulation is available in Ref. [54]. (c) Spin-spin and species-species correlation functions along x : $C_{\sigma\sigma}(r) = \langle v_{s,i+r} v_{s,i} \rangle$ and $C_{ss}(r) = \langle m_{i+r} m_i \rangle$, respectively, for $\beta_1 = 1, \beta_2 = 1.5, D = 0.05, v = 1$, and $\rho_0 = 16$, and calculated in a 2048×128 domain. (d) Diffusion-density state diagram for $\beta_1 = 1, \beta_2 = 1.5$, and $v = 1$. The SRO region exhibits steady states similar to (b). (e–f) Motility-induced pinning for $\beta_1 = 3, D = 0.05, v = 1, \rho_0 = 4$, and several species coupling: (e) $\beta_2 = 1.5$ and (f) $\beta_2 = 2.25$ (colormap as in Fig. 1). A movie (movie 7) of the simulations is available in Ref. [54].

species [Fig. 12(a)], akin to the TSAIM without species-flip (see Sec. IV B). The spin-flip mechanism governed by $W_{\text{flip}}^{(1)}$ is mainly responsible for this spontaneous nucleation which breaks the long-range order characterized by bulk HDPF bands. A new steady state is then formed by left and right flocking clusters arranged in stripes of A and B species along the y -axis [Fig. 12(b)]. This morphology exhibits strong species correlations within each stripe but displays short-range order in spin, like the one-species AIM [20].

We now study this new steady-state formed by the spontaneous nucleation of droplets in the HDPF state and estimate the typical size for the steady-state left and right flocking clusters. Fig. 12(c) shows the spin-spin and the species-species correlation functions, $C_{\sigma\sigma}(r)$ and $C_{ss}(r)$, as defined in Sec. IV B, and calculated in a

2048×128 domain. Akin to the one-species AIM [20], the spin-spin correlation function $C_{\sigma\sigma}(r)$ exhibits an exponential decay to zero with correlation lengths $\xi_x \simeq 110$ and $\xi_y \simeq 10$ along the x and y directions, respectively, demonstrating the short-range order in spin of the new steady state. These correlation lengths, independent of the system size, give a characteristic size to the constitutive flocking clusters. The species-species correlation function $C_{ss}(r)$ does not decay to zero along the x direction and can be expressed as $C_{ss}(r) \sim C_\infty + (1 - C_\infty) \exp(-r/\xi_x)$ with a correlation length $\xi_x \simeq 110$ and $C_\infty \simeq 0.38$, indicating the presence of long-range order in species within the new steady state. To emphasize, spontaneous nucleation of droplets disrupts the HDPF state in both versions of the TSAIM, with and without species flip. However, the resulting steady-state in the TSAIM without species flip exhibits long-range order in spin and short-range order in species, while the TSAIM with species flip displays the opposite behavior: long-range order in species and short-range order in spin.

Fig. 12(d) shows the diffusion-density state diagram for $v = 1, \beta_1 = 1$, and $\beta_2 = 1.5$, computed similarly to the state diagrams displayed in Figs. 11(d–f) but for the hopping rate W_{hop} with $\theta = 1$. The gas and liquid binodals $\rho_g, \rho_l^{(1)}$, and $\rho_l^{(2)}$ decrease with D . For a diffusion constant $D \lesssim 0.1$, the liquid states are no longer stable and the system exhibits a steady-state morphology as depicted in Fig. 12(b), and denoted SRO (short-range ordered spin state) in this state diagram. Akin to the one-species AIM [20], the liquid binodals are no longer defined.

The TSAIM with species flip also exhibits motility-induced interface pinning (MIIP) at large values of β_1 (low temperatures), enhanced in the presence of small diffusion [20], following the same mechanism explained in Sec. IV. Figs. 12(e–f) illustrate this MIIP state for increasing values of β_2 . For $\beta_2 = 0.75$, no MIIP state is observed and the system exhibits a ferromagnetic gas phase (data not shown). For $\beta_2 = 1.5$, the MIIP state is formed by particles of both species, with many particles moving outside this structure and not contributing to the formation of these interfaces [Fig. 12(e)]. For $\beta_2 = 2.25$, the MIIP state is defined by two distinct, high-density pinned interfaces of each species, due to stronger interface pinning and more particles contributing to the formation of these interfaces [Fig. 12(f)]. As demonstrated, in addition to temperature T_1 , temperature T_2 , which governs species flip, also plays a crucial role in the emergence of the MIIP state and determining its morphology. Similarly to TSAIM without species flip (see Sec. IV B), the MIIP states are independent of the initial configuration, and the formation of these interfaces is enhanced when the diffusion D is small compared to the velocity v .

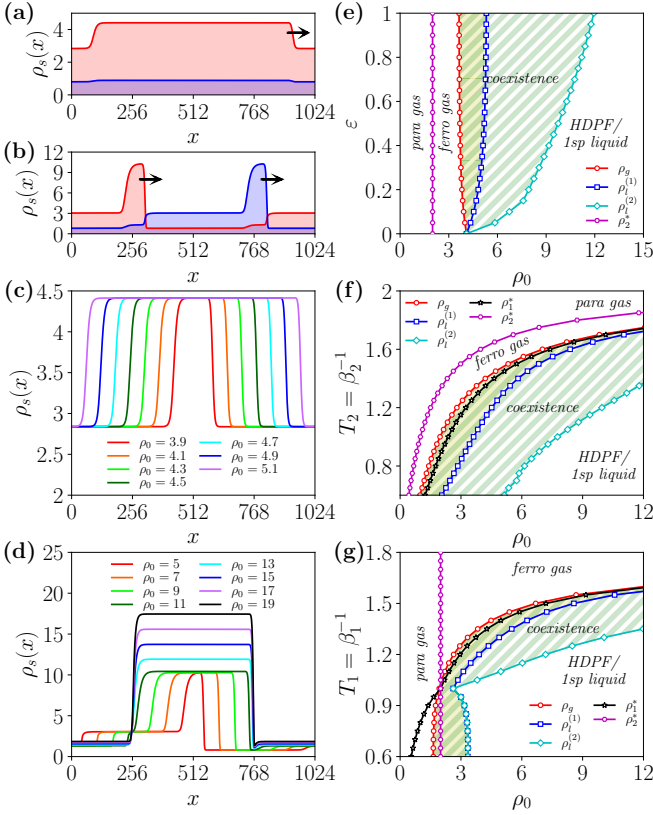


FIG. 13: (color online) Hydrodynamic theory of the TSAIM with species flip ($\gamma_2 = 0.5$). (a–b) Steady state profiles for same density $\rho_0 = 5$ but different initial species magnetization: (a) $m_0 = 5$, and (b) $m_0 = 0$. (c–d) Steady-state density profiles (in PF state) for different densities and initial species magnetization: (c) $m_0 = \rho_0$, and (d) $m_0 = 0$. Parameters: $\beta_1 = 0.75$, $\beta_2 = 0.75$, $\varepsilon = 0.9$, and $L_x = 1024$. (e) Velocity-density state diagram for $\beta_1 = \beta_2 = 0.75$. (e) Temperature T_2 -density state diagram for $\beta_1 = 0.75$ and $\varepsilon = 0.9$. (f) Temperature T_1 -density state diagram for $\beta_2 = 0.75$ and $\varepsilon = 0.9$.

C. Hydrodynamic theory

We now present the results obtained from the hydrodynamic theory derived in Sec. III, via the solution of the Eqs. (9)-(12) with $\gamma_2 \neq 0$. Here, we will restrain to the special case $r_1 = r_2 = r$, leading to $\bar{\gamma}_2/\bar{\gamma}_1 = \gamma_2/\gamma_1 \equiv \gamma$. The non-motile case, for which $\varepsilon = 0$ (i.e. $v = 0$), exhibits only homogeneous stationary solutions: $\rho(x) = \rho_0$, and

$$m = \left(\rho_0 - \frac{r}{2\beta_2} \right) \tanh \frac{2\beta_2 m}{\rho_0}, \quad (17)$$

$$v_s = m \tanh \frac{2\beta_1 v_a}{\rho_0}, \quad (18)$$

$$\left(\rho_0 - \frac{r}{2\beta_1} \right) \sinh \frac{2\beta_1 v_a}{\rho_0} - v_a \cosh \frac{2\beta_1 v_a}{\rho_0}$$

$$+ \gamma \left[v_s \sinh \frac{2\beta_2 m}{\rho_0} - v_a \cosh \frac{2\beta_2 m}{\rho_0} \right] = 0. \quad (19)$$

From Eq. (17), we get a second-order phase transition between a disordered homogeneous solution where $m = 0$ and an ordered homogeneous solution $|m| > 0$. The transition occurs when $2\beta_2 - r/\rho_0$ is larger than 1, i.e. for a density larger than $\rho_2^* = r/(2\beta_2 - 1)$ and for a temperature $T_2 < T_c = 2$. This expression is compatible with the transition line obtained from simulations of the microscopic model and shown in Fig. 10(c). From Eqs. (18)-(19), we get a second-order phase transition between a disordered homogeneous solution where $v_a = 0$ and an ordered homogeneous solution $|v_a| > 0$. The transition occurs for a density larger than ρ_1^* , solution of the equation:

$$\rho_1^* = \frac{r}{2\beta_1 - 1 + \gamma[(\beta_1/\beta_2)M_* \sinh M_* - \cosh M_*]}, \quad (20)$$

with $M_* = 2\beta_2 m_*/\rho_1^*$ where m_* is a stable solution of Eq. (17) with $\rho_0 = \rho_1^*$, i.e. $m_* = 0$ for $\rho_1^* < \rho_2^*$ and $m_* > 0$ for $\rho_1^* > \rho_2^*$. The solution is trivial for $\rho_1^* < \rho_2^*$: $\rho_1^* = r/(2\beta_1 - 1 - \gamma)$, but not analytically tractable for $\rho_1^* > \rho_2^*$. Numerical solutions tell us that ρ_1^* is continuous as function of T_1 and T_2 , but its derivative exhibits a discontinuity at the temperature T_1 such that $\rho_1^*(T_1, T_2) = \rho_2^*(T_2)$, i.e. $T_1 = T_2/(1 + \gamma T_2/2)$.

Phase-separated density profiles can be observed for a positive velocity ($\varepsilon > 0$). Figs. 13(a–d) shows the steady-state density profiles $\rho_s(x)$ in the PF state. Two different initial average species magnetization are considered: $\langle m(x) \rangle = m_0 = \rho_0$ for Figs. 13(a,c) and $\langle m(x) \rangle = m_0 = 0$ for Figs. 13(b,d). Analogous to the results obtained from the simulations of the microscopic model, two kinds of phase-separated density profiles are observed for the same density $\rho_0 = 5$: one-species flocking when starting with $m_0 = \rho_0$ [Fig. 13(a)], akin to the one-species AIM [13], and two-species flocking when starting with $m_0 = 0$ [Fig. 13(b)], where the density $\rho_s(x)$ takes four different values for the same reasons discussed in Fig. 11(b). Figs. 13(c–d) show these steady-state density profiles $\rho_s(x)$ with increasing densities. Starting with $m_0 = \rho_0$, the density profiles are analogous to the one-species AIM [13] [Fig. 13(c)], and starting with $m_0 = 0$, the profiles exhibit phase-separated PF bands similar to Fig. 13(b) for densities $\rho_0 < 11.59$ and a HDPF state for densities $\rho_0 > 11.59$ [Fig. 13(d)].

We determine the binodals from the minimum and maximum density $\rho = \rho_A + \rho_B$ of these phase-separated profiles: $\rho_g^{(1)} = 3.64$ and $\rho_l^{(1)} = 5.30$ when one species is present, and $\rho_g^{(2)} = 3.60$ and $\rho_l^{(2)} = 11.59$ when two species are present in the steady state. As for simulations of the microscopic model, we have $\rho_g^{(1)} \sim \rho_g^{(2)} \equiv \rho_g$ and $\rho_l^{(1)} < \rho_l^{(2)}$. Computing the binodals for several velocities ε and temperatures T_1 and T_2 , we construct the velocity-density state diagram for $\beta_1 = \beta_2 = 0.75$ [Fig. 13(e)], the temperature T_2 -density state diagram for $\varepsilon = 0.9$ and

$\beta_1 = 0.75$ [Fig. 13(f)], and the temperature T_1 -density state diagram for $\varepsilon = 0.9$ and $\beta_2 = 0.75$ [Fig. 13(g)]. We recover the four regions observed with simulations of the microscopic model: paramagnetic gas phase ($\rho_0 < \rho_2^*$), ferromagnetic gas phase ($\rho_2^* < \rho_0 < \rho_g$), coexistence region ($\rho_g < \rho_0 < \rho_l$), and liquid state ($\rho_0 > \rho_l$), where ρ_l can either be $\rho_l^{(1)}$ or $\rho_l^{(2)}$, depending on the initial configuration. This liquid state is characterized by a one-species liquid phase (*1sp liquid*) for $\rho_0 > \rho_l^{(1)}$, or by an HDPF state for $\rho_0 > \rho_l^{(2)}$. However, the coexistence region will be slightly different here: the gas binodal ρ_g will always be between ρ_1^* and ρ_2^* leading to two sub-regions: (i) $\rho_2^* < \rho_g < \rho_1^*$ where a ferromagnetic gas phase ($m > 0$ and $v_a = 0$) coexists with a liquid band ($m > 0$ and $v_a > 0$), and (ii) $\rho_1^* < \rho_g < \rho_2^*$ where a APF state ($m = 0$ and $v_a > 0$) coexists with a liquid band ($m > 0$ and $v_a > 0$). This second subregion is unstable in the presence of fluctuations, leading to the microphase-separated profiles observed in Figs 7(g-h).

VI. RESULTS WITH NON-RECIPROCAL INTERACTIONS ($\gamma_2 = 0$)

In this section, we consider the TSAIM with non-reciprocal interactions (NRTSAIM) which is a minimal microscopic model of non-reciprocal flocking with two species having competing interests: species A aligns with species B with an interaction strength J_{AB} ($0 \leq J_{AB} \leq J_1$) while species B anti-aligns with species A with interaction strength J_{BA} ($-J_1 \leq J_{BA} \leq 0$). We further define the dimensionless variables $\mathcal{J}_{ss'} = J_{ss'}/J_1$ and $\beta_1 = \beta J_1$. Here, we will again consider an equal population of both species, $N_A = N_B = N/2$, i.e. $m_0 = 0$.

For the results presented in this section, we initialize the system in either an ordered or semi-ordered configuration. In an ordered configuration, particles of both species possess the same spin σ , whereas in the semi-ordered configuration, high-density bands of both species are arranged in either a PF or an APF state. If simulations start from a disordered initial configuration in the presence of non-reciprocal frustration, the system tends to remain disordered. This is due to the continuous switching of the spin σ of a particle between its two states (± 1), resulting in a disordered steady state.

A. Steady-state profiles and phase diagrams

In this subsection, we present the results for a hopping rate, given by Eq. (1), with $\theta = 0$ and $D = 1$. First, we consider the non-reciprocal interaction as $\mathcal{J}_{AB} = -\mathcal{J}_{BA} \equiv \mathcal{J}_{NR}$, where the coupling constant of A-particles with B-particles, $\mathcal{J}_{AB} > 0$, is exactly the opposite of the coupling constant of B-particles with A-particles, $\mathcal{J}_{BA} < 0$.

We first analyze the effect of self-propulsion ($\varepsilon > 0$).

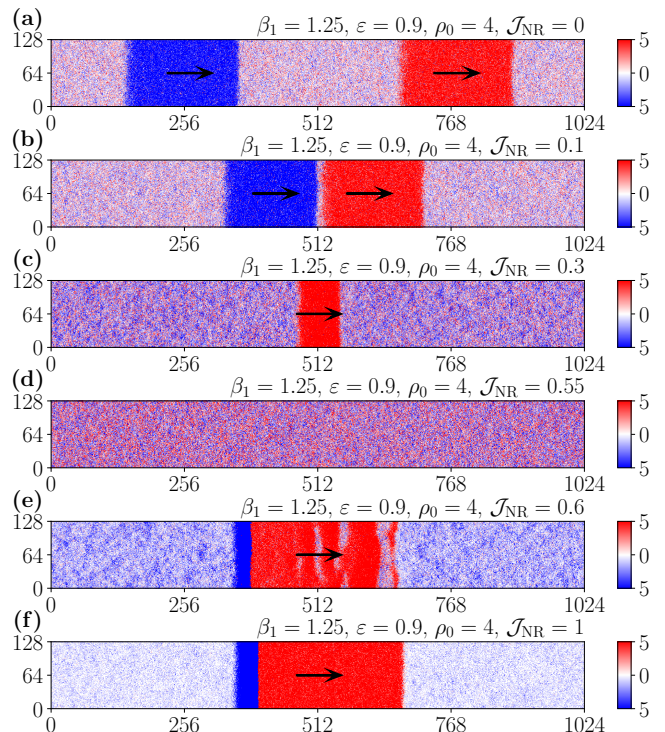


FIG. 14: (color online) Steady-state snapshots of the NRTSAIM for $\beta_1 = 1.25$, $\varepsilon = 0.9$, $\rho_0 = 4$, and increasing non-reciprocal interaction: (a) $\mathcal{J}_{NR} = 0$, (b) $\mathcal{J}_{NR} = 0.1$, (c) $\mathcal{J}_{NR} = 0.3$, (d) $\mathcal{J}_{NR} = 0.55$, (e) $\mathcal{J}_{NR} = 0.6$, and (f) $\mathcal{J}_{NR} = 1$ in a 1024×128 domain (colormap as in Fig. 1). A movie (movie 8) of the simulations is available in Ref. [54].

Starting from the same initial configuration, Fig. 14 shows all the possible steady-state density configurations exhibited by the NRTSAIM for large self-propulsion $\varepsilon = 0.9$ as the strength of the non-reciprocal interaction \mathcal{J}_{NR} is increased. Fig. 14(a) and Fig. 14(b) exhibit a flocking state of two species (in a PF state) for $\mathcal{J}_{NR} = 0$ and $\mathcal{J}_{NR} = 0.1$, respectively. In Fig. 14(b), the B-band (blue) appears narrower and denser compared to the A-band whereas in Fig. 14(a), both bands exhibit equal width and density due to the absence of inter-species interactions. This occurs because the slight increase in the non-reciprocity increases the velocity of the B-band and propels it near to the opposite extremity of the A-band (relative to the band propulsion direction) as B-particles respond to the emerging non-reciprocal environment. Despite the growing strength of non-reciprocal interactions, the two-species flocking behavior persists up to a point, after which the system transitioned to a flocking state of only species A, as shown in Fig. 14(c), for $\mathcal{J}_{NR} = 0.3$. However, as we increase \mathcal{J}_{NR} further, a transition to a fully disordered state occurs in both species [Fig. 14(d)], followed by run-and-chase dynamics at higher values of \mathcal{J}_{NR} [Figs. 14(e-f)]. This run-and-chase dynamics emerges from the nucleation of an A-band in the gas phase in front of the B-band, since A-

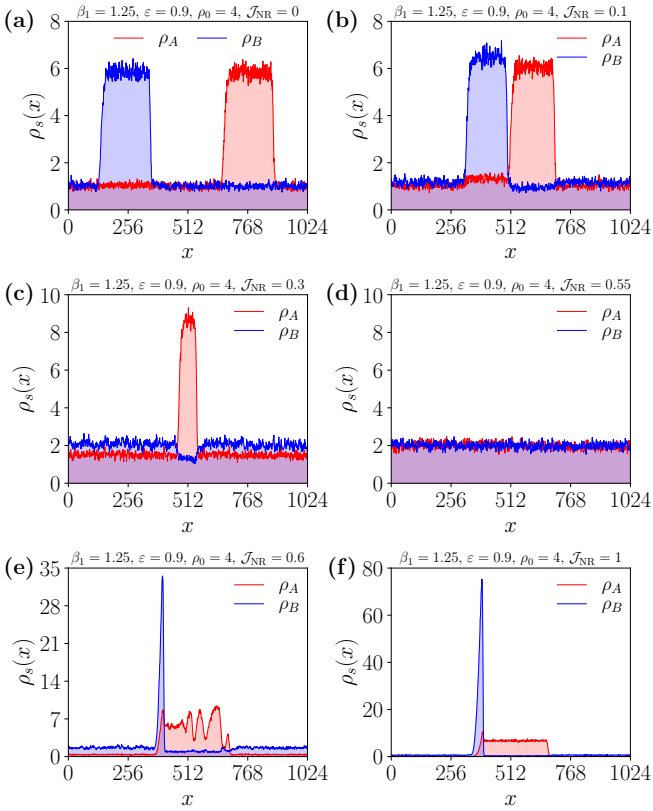


FIG. 15: (color online) Steady-state density profiles of the NRTSAIM for increasing \mathcal{J}_{NR} , obtained from the density snapshots shown in Fig. 14 by integrating along the y -axis.

particles tend to align with B-particles. The B-particles tend to avoid them because of the non-reciprocal interaction, resulting in a substantial accumulation of B-particles, which leads to a denser B-band, and a slowing down of the B-band velocity. Therefore, the arrangement shown in Fig. 14(f) exemplifies a highly efficient non-reciprocal configuration, facilitating the B-particles to maintain the *maximum distance* from the chasing A-particles. The velocity $c \sim 1.96$ of the flocking bands [Fig. 14(a–b)] is larger than the self-propulsion velocity of the particles $v = 2D\varepsilon = 1.8$ for small non-reciprocity, as also observed in the one-species AIM [13]. However, in the run-and-chase state [Fig. 14(e–f)], the velocity $c \sim 1.64$ of the B-band is smaller than v since the non-reciprocal interaction slows down the dynamics of the B-band.

Fig. 14 qualitatively evaluates the NRTSAIM states via steady-state snapshots as the non-reciprocal interaction strength increases. This qualitative assessment is complemented by the corresponding density profiles shown in Fig. 15, which provides a more quantitative picture of the phenomenon. We observe two identical yet distinct density profiles of species A and B in Fig. 15(a) as the interspecies interaction is zero. The profiles signify that the system is in the liquid-gas coexistence regime, where each

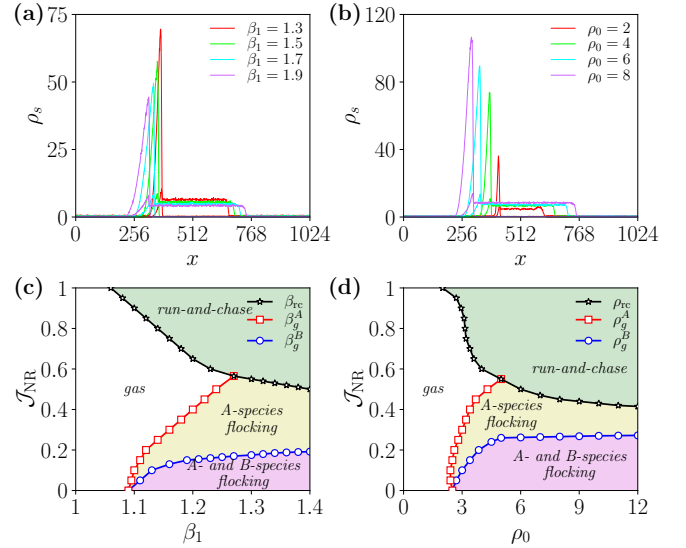


FIG. 16: (color online) Profiles and state diagrams for the NRTSAIM (I). (a–b) Steady-state density profiles of species A (flat profiles) and species B (sharp peaks), shown for (a) different β_1 with fixed $\rho_0 = 4$, and (b) varying ρ_0 with fixed $\beta_1 = 1.25$. Parameters: $\varepsilon = 0.9$, $\mathcal{J}_{\text{NR}} = 1$, $L_x = 1024$, $L_y = 128$. (c) $(\mathcal{J}_{\text{NR}}, \beta_1)$ state diagram for $\rho_0 = 4$ and $\varepsilon = 0.9$; and (d) $(\mathcal{J}_{\text{NR}}, \rho_0)$ state diagram for $\beta_1 = 1.25$ and $\varepsilon = 0.9$.

species exhibits order solely within its respective band while remaining disordered elsewhere. For $\mathcal{J}_{\text{NR}} = 0.1$ [Fig. 15(b)], with the emergence of non-reciprocity, the liquid density within the B-profile surpasses that of the corresponding A-profile, as B-particles try to move away from the high-density A-band. However, within the B-band, A-particles align with B-particles, both sharing the same spin state σ and moving in the same direction. In contrast, within the A-band, B-particles are anti-aligned with A-particles, moving in the opposite direction with an opposite spin state. A similar effect occurs in the one-species flocking band of species A [Fig. 15(c)] for $\mathcal{J}_{\text{NR}} = 0.3$], where non-reciprocity causes contrasting behaviors in B-particles: they are in a disordered state outside the A-band, but in an anti-aligned ordered state inside the band. With a continued increase in non-reciprocal frustration, both species transition into a disordered state [Fig. 15(d)]. Subsequently, a run-and-chase state emerges for large \mathcal{J}_{NR} [Figs. 15(e–f)] where the bands of each species are coupled. In this run-and-chase state, the maximum density of the B-profile increases with \mathcal{J}_{NR} as an increasing number of B-particles try to escape contact with the moving A-band.

To illustrate the influence of density and noise on the run-and-chase state, we present the steady-state density profiles of species A and B for $\mathcal{J}_{\text{NR}} = 1$ in Fig. 16(a–b). Regardless of whether system density increases at fixed noise or β_1 increases at fixed density, the system remains in the run-and-chase state, without transitioning to an ordered phase. As β_1 is increased, with fixed density ρ_0 ,

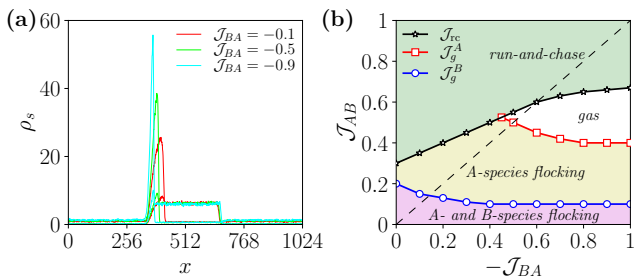


FIG. 17: (color online) Profiles and state diagrams for the NRTSAIM (II). (a) Steady-state density profiles of species A (flat profiles) and species B (sharp peaks) for different values of \mathcal{J}_{BA} and fixed $\mathcal{J}_{AB} = 0.7$, $\beta_1 = 1.25$, $\varepsilon = 0.9$, $\rho_0 = 4$ in a 1024×128 domain. (b) $(\mathcal{J}_{AB}, -\mathcal{J}_{BA})$ state diagram for $\beta_1 = 1.25$, $\varepsilon = 0.9$, and $\rho_0 = 4$. The dotted line represents $\mathcal{J}_{AB} = -\mathcal{J}_{BA}$ as a guide to the eyes.

the run-and-chase state exhibits wider A and B-bands and a decrease in the maximal density of each band, due to stronger intra-species interactions [Fig. 16(a)]. As the total density is increased, with fixed β_1 , the run-and-chase state shows broader but denser bands [Fig. 16(b)]. A higher density leads more B-particles to move within the narrow, high-density B-band to avoid the expanding A-band. However, since A-particles are aligned with B-particles, the density of A-particles noticeably increases within the high-density B-band.

To comprehensively illustrate the influence of noise and density on the NRTSAIM steady states, we construct the $(\mathcal{J}_{NR}, \beta_1)$ and $(\mathcal{J}_{NR}, \rho_0)$ state diagrams, depicted in Figs. 16(c-d). These state diagrams exhibit four regions representing the following states: A- and B-species flocking, A-species flocking, disordered gas, and run-and-chase states. When $\mathcal{J}_{NR} = 0$, denoting the absence of inter-species interaction, we observe the emergence of flocking bands of both species, as noise decreases or density increases. As \mathcal{J}_{NR} is increased for $\beta_1 = 1.25$ and $\rho_0 = 4$, the system goes through all the possible states of the NRTSAIM, as shown in Fig. 14. As β_1 and ρ_0 are increased, the transition from a flocking state to the disordered state occurs at larger values of \mathcal{J}_{NR} , while the transition to the run-and-chase state appears at smaller values of \mathcal{J}_{NR} , as this state becomes more favorable even with weaker non-reciprocal coupling.

We now shift our focus to the scenario where the magnitudes of the inter-species coupling strengths may differ from each other ($\mathcal{J}_{AB} \neq -\mathcal{J}_{BA}$, but keeping $\mathcal{J}_{AB} \geq 0$ and $\mathcal{J}_{BA} \leq 0$). We observe that the impact of \mathcal{J}_{AB} stands in stark contrast to that of \mathcal{J}_{BA} . By maintaining a constant $\mathcal{J}_{AB} = 0.7$, the system exhibits a run-and-chase state for any values of \mathcal{J}_{BA} . An increase of $|\mathcal{J}_{BA}|$ further consolidates the run-and-chase state, as evidenced by the density profiles of the B-species [Fig. 17(a)].

Subsequently, we construct a $(\mathcal{J}_{AB}, -\mathcal{J}_{BA})$ state diagram in Fig. 17(b) to illustrate the comparative influence of \mathcal{J}_{AB} and \mathcal{J}_{BA} in defining the steady-states of the

NRTSAIM. To illustrate the effect of nonreciprocity, let us move horizontally in the state diagram keeping \mathcal{J}_{AB} constant, from $\mathcal{J}_{BA} = 0$ to $\mathcal{J}_{BA} = -1$ (increasing the anti-alignment interaction). For small \mathcal{J}_{AB} , the system exhibits a two-species or one-species flocking state, illustrated in Figs. 14(a-c). For $\mathcal{J}_{AB} \geq 0.7$, regardless of the magnitude of the coupling \mathcal{J}_{BA} , the system consistently manifests a run-and-chase state, as shown in Figs. 14(e-f), where the velocity of the B-band slowly decreases with $-\mathcal{J}_{BA}$. On the other hand, if we now move vertically in the state diagram keeping \mathcal{J}_{BA} constant, the system transitions from a two-species flocking state to a run-and-chase state, via a one-species flocking state, when \mathcal{J}_{AB} is increased. For large \mathcal{J}_{BA} , this transition occurs through an intermediate disordered gas state. Moving along the diagonal dotted line $\mathcal{J}_{AB} = -\mathcal{J}_{BA}$, from the bottom-left to the upper-right corners, we go through the steady states as presented in Fig. 14. Hence, it appears that \mathcal{J}_{AB} assumes a more critical role in determining the emergence of the steady states than \mathcal{J}_{BA} . To emphasize, a strong preference of species A to B propels the system toward the run-and-chase state, even for a slight aversion of B towards A.

B. Metastability and MIIP in the NRTSAIM

Similarly to our analysis of reciprocal TSAIM (without and with species flip, discussed in Secs. IV B and V B, respectively), we now present an analysis of the stability of the NRTSAIM steady states and confirm that all these steady states are metastable due to the spontaneous nucleation of opposite spin droplets [20]. In Fig. 18, starting from an initial PF configuration where particles obey the hopping rate W_{hop} , defined by Eq. (1), with $\theta = 1$ and a small D , we demonstrate the metastability of the run-and-chase state when a droplet spontaneously nucleates in the A-band (red) [Figs. 18(a-c)]. Due to the strongly non-reciprocal environment, B-particles initially accumulate away from the approaching A-particles, attempting to form a typical run-and-chase state characteristic of large \mathcal{J}_{NR} . However, the spontaneous emergence of the droplet disrupts this structure [Figs. 18(d-e)], causing the system to transition to a short-range gas phase [Fig. 18(f)]. A movie (movie 9) showing the similar fate of an HDPF state in a square geometry is available in Ref. [54].

Akin to one-species AIM [20] and the reciprocal TSAIM without or with species flip [see Figs. 5(e-f) and Figs. 12(e-f)], the NRTSAIM also exhibits a motility-induced interface pinning (MIIP) state at low temperature, as shown in Fig. 19. At large \mathcal{J}_{NR} , the MIIP clusters of species B are destroyed. Starting from an initial configuration with two high-density bands of A and B species, the system evolves under various \mathcal{J}_{NR} values. At initial times, spontaneously excited opposite polarity droplets inside the bands of each species act as the pinning sites. Consequently, the system promptly undergoes

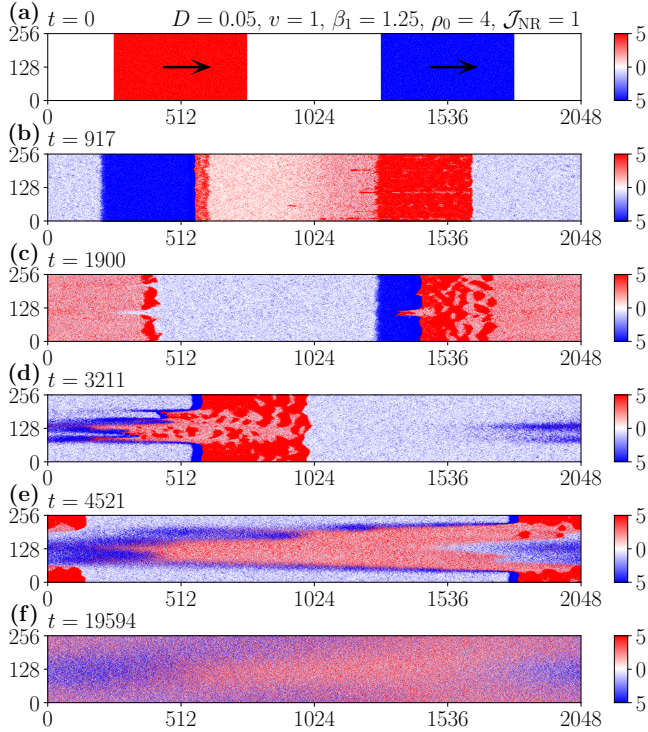


FIG. 18: (color online) Metastability in the NRTSAIM. Time evolution from a phase-separated initial configuration, demonstrating the metastability of the run-and-chase state, for $\beta_1 = 1.25$, $D = 0.05$, $v = 1$, $\rho_0 = 4$, and $\mathcal{J}_{\text{NR}} = 1$, in a 2048×256 domain (colormap as in Fig. 1).

the MIIP transition for each species separately [Fig. 19(a) and Fig. 19(d), for $\mathcal{J}_{\text{NR}} \leq 0.3$], similar to the reciprocal TSAIM, where those small droplets gradually form multiple pinned elongated clusters that merge over time into a single, narrow, high-density elongated cluster. These clusters are jammed configurations divided by an interface: the right half consists of particles with $\sigma = -1$, and the left half consists of particles with $\sigma = +1$. When a particle crosses the interface at very low temperatures, it flips its spin state and consequently its self-propulsion direction, causing it to return and thereby pinning the interface.

However, for $\mathcal{J}_{\text{NR}} \geq 0.4$, the MIIP morphology observed in Figs. 19(a,d) becomes unsustainable, and only the MIIP clusters of species A persist, while the MIIP clusters of species B are destroyed over time [Figs. 19(b,e-f)]. As \mathcal{J}_{NR} increases, the anti-alignment strength between species B and A particles also increases. During the formation of multiple MIIP clusters for both species, a significant number of unpinned A and B particles also move in the background. Because the MIIP clusters are jammed, particle diffusion mainly occurs from the top and bottom edges of the clusters. Now, when species A particles approach a MIIP cluster of species B, a $\sigma = +1$ ($\sigma = -1$) A-particle encounters the $\sigma = +1$ ($\sigma = -1$) edges of the cluster from the left (the right). However,

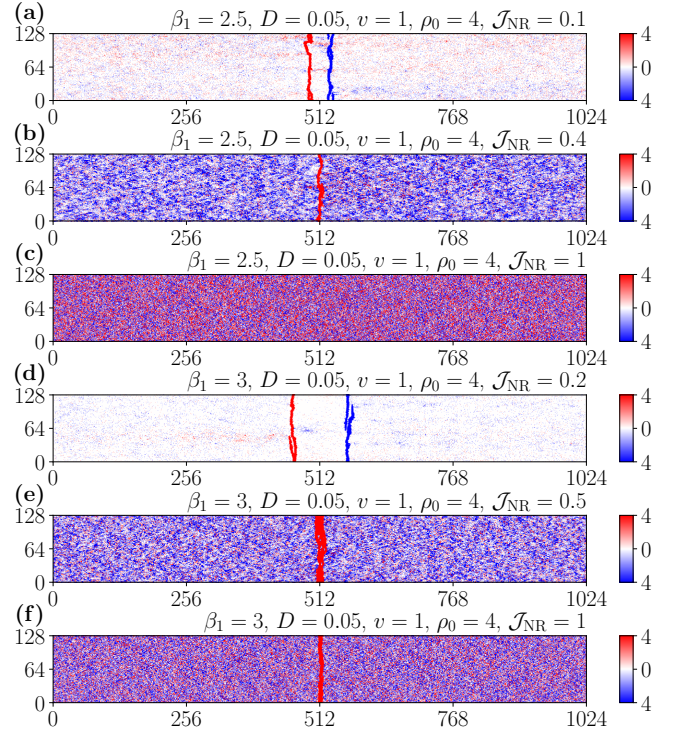


FIG. 19: (color online) Motility-induced pinning in the NRTSAIM for increasing \mathcal{J}_{NR} and fixed (a–c) $\beta_1 = 2.5$; and (d–f) $\beta_1 = 3$. Parameters: $D = 0.05$, $v = 1$, $\rho_0 = 4$, $L_x = 1024$, and $L_y = 128$ (colormap as in Fig. 1). A movie (movie 10) of the simulations is available in Ref. [54].

since species B anti-aligns with species A, the B-particle flips its spin state σ and leaks out of the cluster (leaking from a jammed MIIP cluster occurs only when a $\sigma = +1$ particle flips to $\sigma = -1$, or vice versa). This leakage occurs at both edges, leading to the gradual reduction and eventual destruction of the B-species MIIP clusters. In contrast, when a MIIP cluster of species A is approached by species B particles, the A-particles, which prefer to align with B particles, retain their spin state and do not flip, preventing any leakage. However, when the non-reciprocal frustration is strong [compare Figs. 19(c) and 19(f)], the survival of the A-species MIIP cluster becomes dependent on β_1 , as a large β_1 is known to facilitate pinning of the domain interface [20]. Hence, for sufficiently large \mathcal{J}_{NR} , a larger β_1 is required to observe a stable MIIP cluster.

C. Non-motile NRTSAIM ($\varepsilon = 0$)

We now examine the scenario of non-motile NRTSAIM ($\varepsilon = 0$), where particles of both species only diffuse. In the absence of non-reciprocity ($\mathcal{J}_{\text{NR}} = 0$), a phase transition occurs from a disordered state at low density and large noise to an ordered state at large density and low noise. With the introduction of non-reciprocity via

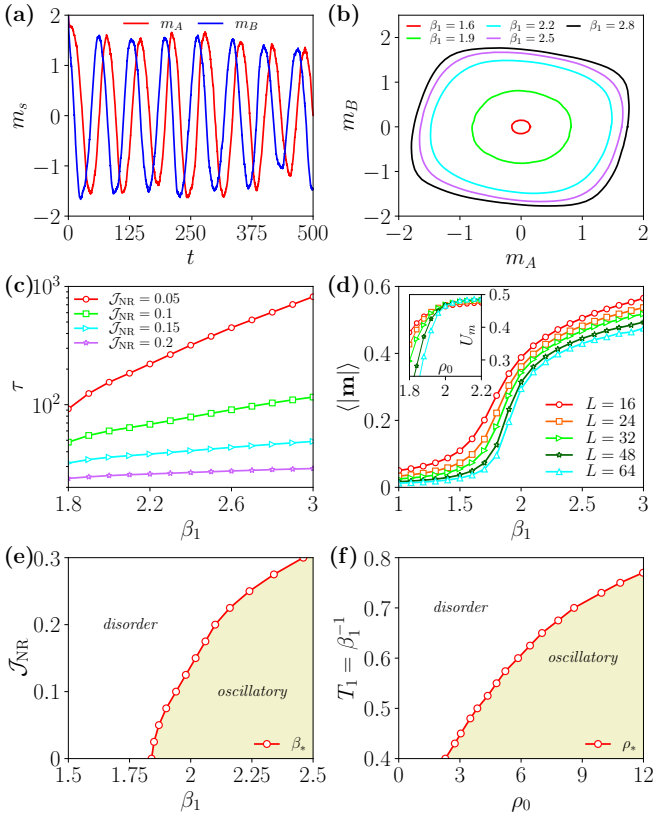


FIG. 20: (color online) Non-motile NRTSAIM ($\varepsilon = 0$): (a) Time-evolution of m_A and m_B exhibiting an oscillatory state for $\beta_1 = 2.2$, $\rho_0 = 4$, and $\mathcal{J}_{\text{NR}} = 0.1$ in a 64×64 domain. (b) Phase portrait for $\rho_0 = 4$, $\mathcal{J}_{\text{NR}} = 0.1$, and increasing β_1 in a 64×64 domain. (c) Oscillation period vs β_1 for several \mathcal{J}_{NR} couplings and $\rho_0 = 4$. (d) Mean value and Binder cumulant (inset) of the vector order parameter $\mathbf{m} = (m_A, m_B)$ vs β_1 for $\rho_0 = 4$, $\mathcal{J}_{\text{NR}} = 0.1$, and several system sizes. The transition occurs at $\beta_* = 1.94$. (e) $(\mathcal{J}_{\text{NR}}, \beta_1)$ state diagram for $\rho_0 = 4$, and (f) (T_1, ρ_0) state diagram for $\mathcal{J}_{\text{NR}} = 0.1$.

\mathcal{J}_{NR} , we witness the emergence of a dynamical oscillatory state (or swap state) [35], characterized by oscillations in the magnetizations of both species over time [Fig. 20(a)], where m_A is in late quadrature with m_B . The magnitudes of these oscillations fluctuate over time, and generally increase with β_1 and decrease with \mathcal{J}_{NR} . Fig. 20(b) shows the phase portraits (m_A, m_B) and illustrates the transition from the disordered state to the oscillatory state. In the disordered state, $m_A = m_B = 0$ is the only stable fixed point, while the oscillatory state is depicted by stable limit cycles, with their area increasing as β_1 increases. Furthermore, the time period of these oscillations τ increases exponentially with β_1 , and decreases with \mathcal{J}_{NR} [Fig. 20(c)]. Indeed, a longer period (signifying stronger ordering) arises from weaker noise (larger β_1) and low non-reciprocal strength.

To characterize the transition points between the disordered state and the oscillatory state, we define a vector

order parameter $\mathbf{m} = (m_A, m_B)$. Fig. 20(d) shows the mean value of this order parameter $|\mathbf{m}|$ as a function of β_1 for several system sizes, characteristic of a transition between a disordered state and a quasi-ordered state [57]. The inverse temperature β_* at which this disordered/oscillatory transition occurs is determined by the Binder cumulant of the vector order parameter $U_m = 1 - \langle \mathbf{m}^4 \rangle / 2 \langle \mathbf{m}^2 \rangle^2$, with $\mathbf{m}^2 = m_A^2 + m_B^2$, for several system sizes [inset of Fig. 20(d)]. The Binder cumulant is independent of the system size only at the transition point [55], which gives $\beta_* = 1.94$ for $\rho_0 = 4$ and $\mathcal{J}_{\text{NR}} = 0.1$. By repeating this procedure for varying ρ_0 and \mathcal{J}_{NR} , we compute the $(\mathcal{J}_{\text{NR}}, \beta_1)$ and the (T_1, ρ_0) state diagrams, shown in Figs. 20(e-f), respectively, displaying two steady-states: the disordered and the oscillatory states. However, for $\mathcal{J}_{\text{NR}} = 0$ in Fig. 20(e), the transition occurs between the disordered and the ordered states, where the ordered state can be interpreted as an oscillatory state with an infinite oscillation period. For any nonzero \mathcal{J}_{NR} , regardless of how small, the oscillation period does not diverge at a finite β_1 value, showing that no ordered state can be reached [Fig. 20(c)].

D. Hydrodynamic theory

Next, we present the results derived from the hydrodynamic theory of the NRTSAIM by solving Eqs. (13) and (14). In this section, we will keep the analytical study of these two transitions as general as possible, considering all \mathcal{J}_{AB} and \mathcal{J}_{BA} couplings, and the numerical solutions will be shown for $\mathcal{J}_{AB} = -\mathcal{J}_{BA} = \mathcal{J}_{\text{NR}}$.

Fig. 21 shows the one-dimensional steady-state density profiles of the NRTSAIM for increasing \mathcal{J}_{NR} which resemble those shown in Fig. 15, obtained from simulations of the microscopic model: flocking of species A and B at small \mathcal{J}_{NR} [Figs. 21(a-b)], flocking of only species A at intermediate \mathcal{J}_{NR} [Figs. 21(c-d)], and a run-and-chase behavior at large \mathcal{J}_{NR} [Figs. 21(e-f)]. Analogous to the microscopic simulations, the band velocity of the flocking states is larger than the self-propulsion velocity ($c/v \sim 1.17$ for $\mathcal{J}_{\text{NR}} = 0.1$), whereas the band velocity of the run-and-chase states is smaller ($c/v \sim 0.94$ for $\mathcal{J}_{\text{NR}} = 1$). By examining steady-state profiles for various \mathcal{J}_{NR} , β_1 , and ρ_0 , we obtain qualitatively similar $(\mathcal{J}_{\text{NR}}, \beta_1)$ and $(\mathcal{J}_{\text{NR}}, \rho_0)$ state diagrams for $\varepsilon = 0.9$ in Figs. 22(a-b), akin to those from simulations of the microscopic model shown in Figs. 16(c-d).

The non-motile NRTSAIM, for which $\varepsilon = 0$, i.e. $v = 0$, exhibit only homogeneous solutions: the Eq. (13) for densities gives $\rho_s(x, t) = \rho_0/2$ and the Eq. (14) for magnetizations becomes

$$\frac{\dot{m}_s}{\gamma_s} = \left(\frac{\rho_0}{2} - \frac{r_1}{2\beta_1} \right) \sinh \frac{2\beta_1 \mu_s}{\rho_0} - m_s \cosh \frac{2\beta_1 \mu_s}{\rho_0}, \quad (21)$$

with $m_s(x, t) = m_s(t)$, and $\mu_s = m_s + \mathcal{J}_{s,-s} m_{-s}$. Stationary magnetizations are then solutions of the following

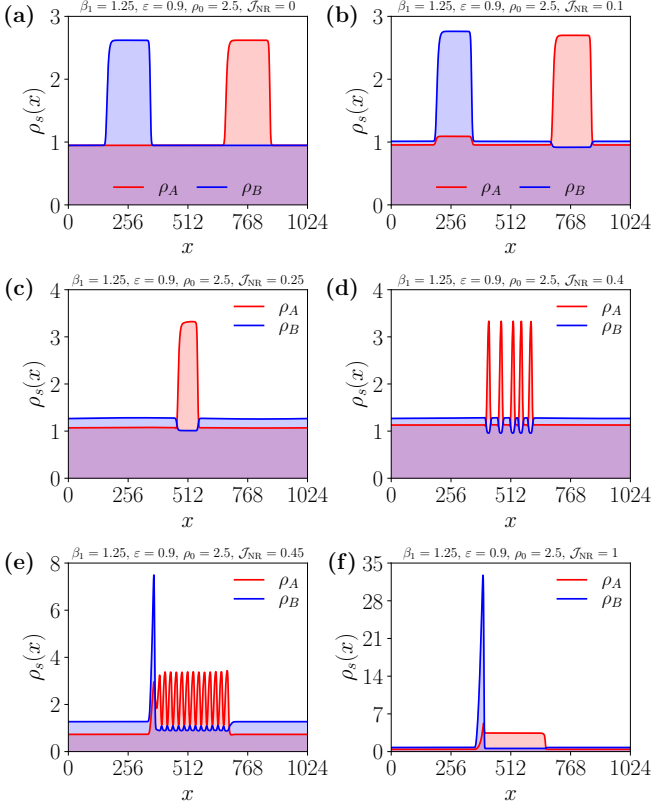


FIG. 21: (color online) Hydrodynamic theory for the NRTSAIM. Steady-state density profiles of the NRTSAIM for $\beta_1 = 1.25$, $\varepsilon = 0.9$, $\rho_0 = 2.5$, $L_x = 1024$, and increasing \mathcal{J}_{NR} : (a) $\mathcal{J}_{\text{NR}} = 0$, (b) $\mathcal{J}_{\text{NR}} = 0.1$, (c) $\mathcal{J}_{\text{NR}} = 0.25$, (d) $\mathcal{J}_{\text{NR}} = 0.4$, (e) $\mathcal{J}_{\text{NR}} = 0.45$, and (f) $\mathcal{J}_{\text{NR}} = 1$.

coupled equations:

$$m_s = \left(\frac{\rho_0}{2} - \frac{r_1}{2\beta_1} \right) \tanh \frac{2\beta_1 \mu_s}{\rho_0}. \quad (22)$$

This system of equations allows two possible solutions: a disordered homogeneous solution ($m_A = m_B = 0$) and ordered homogeneous solutions ($|m_A| > 0$ and $|m_B| > 0$, with $m_A \neq m_B$). Due to non-reciprocal interactions, the transitions where the disordered solution becomes unstable and the homogeneous solutions are stable do not occur at the same density and temperature [35].

Between these two transitions, the magnetizations m_A and m_B exhibit an oscillatory nature [Fig. 22(c)], where m_A is in quadrature with m_B . Fig. 22(d) shows the phase portraits (m_A, m_B) of these stationary and non-stationary solutions as a function of β_1 , for fixed $\rho_0 = 2.5$ and $\mathcal{J}_{\text{NR}} = 0.1$. For $\beta_1 < 1.4$, the disordered solution $m_A = m_B = 0$ is stable. At higher β_1 ($1.4 < \beta_1 < 1.71$), the disordered and ordered solutions are unstable, and the system exhibits a stable limit cycle. For $\beta_1 > 1.71$, the ordered solutions are stable, giving the emergence of four fixed points due to the symmetries of Eq. (22).

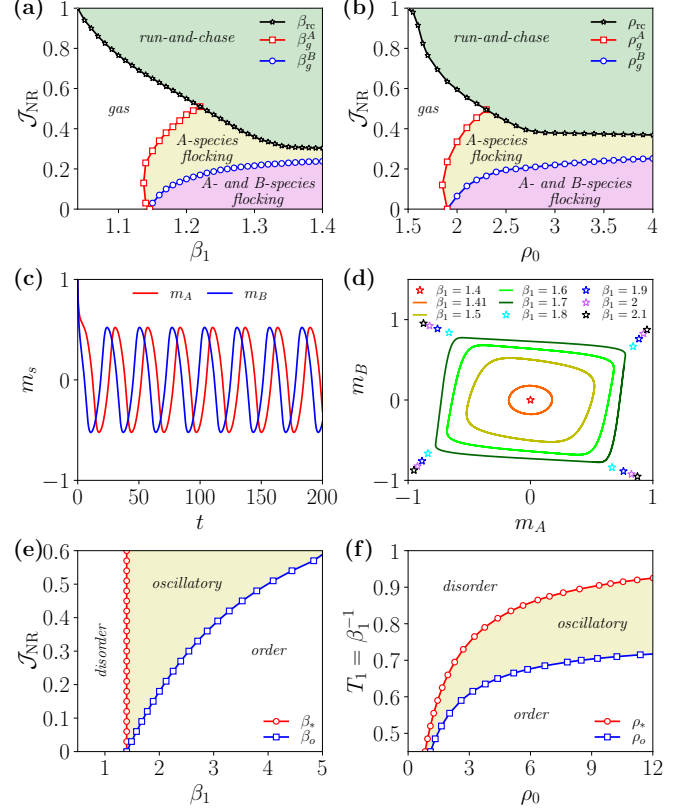


FIG. 22: (color online) Hydrodynamic theory for the NRTSAIM for (a-b) $\varepsilon = 0.9$ and (c-f) $\varepsilon = 0$. (a) ($\mathcal{J}_{\text{NR}}, \beta_1$) state diagram for $\rho_0 = 2.5$, and (b) ($\mathcal{J}_{\text{NR}}, \rho_0$) state diagram for $\beta_1 = 1.25$. (c) Time evolution of m_A and m_B exhibiting an oscillatory state for $\beta_1 = 1.5$, $\rho_0 = 2.5$, and $\mathcal{J}_{\text{NR}} = 0.1$. (d) Phase portraits for $\rho_0 = 2.5$, $\mathcal{J}_{\text{NR}} = 0.1$, and increasing β_1 . (e) ($\mathcal{J}_{\text{NR}}, \beta_1$) state diagram for $\rho_0 = 2.5$, and (f) temperature-density state diagram for $\mathcal{J}_{\text{NR}} = 0.1$.

Furthermore, the period of the oscillatory states follows the same trend as in the simulations of the microscopic model: increasing with β_1 and decreasing with \mathcal{J}_{NR} but diverging at the oscillatory/order transition.

We first derive the disorder/oscillatory transition line, corresponding to a Hopf bifurcation [35], considering a perturbation to the disordered solution: $m_s(t) = \delta m_s(t)$. Keeping only the linear terms in δm_s in Eq. (21), we get

$$\frac{\delta \dot{m}_s}{\gamma_s} = \left(\beta_1 - \frac{r_1}{\rho_0} \right) \delta \mu_s - \delta m_s, \quad (23)$$

with $\delta \mu_s = \delta m_s + \mathcal{J}_{s,-s} \delta m_{-s}$. This equation can be rewritten in a matrix form $\delta \dot{m}_s / \gamma_s = M_{ss'} \delta m_{s'}$, with the diagonal matrix elements $M_{ss} = \beta_1 - 1 - r_1 / \rho_0$ and the off-diagonal matrix elements $M_{s,-s} = (\beta_1 - r_1 / \rho_0) \mathcal{J}_{s,-s}$. We denote λ_{\pm} the two eigenvalues of M , and the evolution of the perturbation is dictated by the sign of the real

part of

$$\lambda_{\pm} = \beta_1 - 1 - \frac{r_1}{\rho_0} \pm i \left| \beta_1 - \frac{r_1}{\rho_0} \right| \sqrt{-\mathcal{J}_{AB}\mathcal{J}_{BA}}. \quad (24)$$

The disordered state becomes unstable when $\beta_1 - 1 - r_1/\rho_0 > 0$, i.e. for a density larger than $\rho_* = r_1/(\beta_1 - 1)$. This transition is then independent of \mathcal{J}_{AB} and \mathcal{J}_{BA} couplings, as soon as the product $\mathcal{J}_{AB}\mathcal{J}_{BA}$ is negative.

We now study the oscillatory/order transition which occurs when Eq. (22) exhibits stable positive stationary solutions. For $\mathcal{J}_{AB} = \mathcal{J}_{BA} = 0$, i.e. with $\mu_s = m_s$, this transition occurs when $\beta_1 - r_1/\rho_0$ is larger than 1, i.e. for a density larger than ρ_* , telling that no oscillatory state is observed without inter-species interactions. In the presence of non-reciprocal interactions, the stability criterion for an ordered solution (m_A, m_B) , derived in appendix E, reads

$$m_s^2 \geq m_o^2 \equiv \left(\frac{\rho_0}{2} - \frac{\rho_0 + r_1}{2\beta_1} \right) \left(\frac{\rho_0}{2} - \frac{r_1}{2\beta_1} \right), \quad (25)$$

giving a maximal extension for the limit circles shown in Fig 22(d).

The $(\mathcal{J}_{NR}, \beta_1)$ and (T_1, ρ_0) state diagrams, obtained by solving numerically Eq. (21), are shown in Figs. 22(e) and 22(f), respectively. The two disorder/oscillatory (β_* or ρ_*) and oscillatory/order (β_o or ρ_o) transition lines delimit the state diagram into three regions, revealing the presence of three distinct states: the disordered state, the oscillatory state, and the ordered state, reflecting the phase portraits shown in Fig 22(d).

However, it is important to note that in our numerical simulations [Fig. 20(b)], we do not observe any ordered state for any nonzero values of \mathcal{J}_{NR} , even at large β_1 . A similar observation is reported in the non-reciprocal Ising model [58], where the oscillatory and ordered states predicted by the mean-field description are absent, destroyed for any amount of non-reciprocity, in the 2D numerical simulations. In 3D, however, the swap state survives, likely due to reduced fluctuations, but the ordered state is eventually destroyed by non-reciprocity. In numerical simulations of our microscopic model, the oscillatory state persists [Fig. 20(e-f)], likely because particles can still diffuse when $\varepsilon = 0$, which stabilizes the oscillatory state.

VII. DISCUSSION

To summarize, we have systematically analyzed a multi-species flocking model with discrete symmetry, the two-species active Ising model (TSAIM), which serves as a discrete-symmetry counterpart of the continuous-symmetry two-species Vicsek model (TSVM) [33]. Driven by recent interests [16–20] in how complex and heterogeneous interactions influence active matter systems, we examine both reciprocal and non-reciprocal in-

teractions between particles of different species, as well as the potential for a particle's species to flip from one species to another.

The flocking transition in the TSAIM with reciprocal interaction between species (without species flip) possesses many similarities with both the one-species AIM [13] and the TSVM [33]: it exhibits a liquid-gas phase transition and displays macrophase separation in the coexistence region [13] where single dense liquid bands of the two species propagate on a gaseous background either in a parallel flocking (PF) state in which the two bands of the two species propagate in the same direction, or in an antiparallel flocking (APF) state in which the bands of species A and species B move in opposite directions [33]. In the coexistence region, stochastic transitions between the PF and the APF states, as they can be observed in the TSVM [33], are absent in the TSAIM, and in the infinite-size limit, the system always relaxes to the PF state starting from a disordered initial condition. At large densities, the TSAIM exhibits a bistable behavior where both the HDPF and liquid APF states are stable depending on the initial condition. The liquid APF state is thermodynamically stable, corresponding to a discrete version of the TSVM liquid state, while the HDPF state emerges due to the discrete nature of the dynamics, i.e. due to normal density fluctuations, and has not been observed in previous flocking models.

The introduction of species inter-conversion in the TSAIM, which corresponds to an active extension of the equilibrium Ashkin-Teller model, further enriches the dynamical behavior of the system, leading to a wider range of steady-state phases: a spin and species-disordered paramagnetic gas phase, a spin-disordered but species-ordered ferromagnetic gas phase, a coexistence region, and a liquid state. The coexistence region can be further divided into three subregions: a ferromagnetic gas phase coexisting with a macrophase-separated liquid band, a paramagnetic gas phase coexisting with a macrophase-separated liquid band, and a paramagnetic gas phase coexisting with microphase-separated liquid bands, which have not been observed in flocking models with discrete symmetry, including the TSAIM without species flip. Thus, species-flip dynamics significantly broaden the range of steady-state phases, with the interplay between initial species composition and density playing a crucial role.

Finally, our investigation of the NRTSAIM reveals the emergence of a highly efficient non-reciprocal dynamical state, termed as the *run-and-chase* state, when non-reciprocal frustration becomes significant. In this state, A-particles chase B-particles to align with them while B-particles avoid due to non-reciprocal interactions. This leads to a substantial accumulation of B-particles at the opposite end of the advancing A-band, allowing B-particles to maintain the maximum distance from the pursuing A-particles. This run-and-chase state can be regarded as the non-reciprocal discrete-symmetry counterpart of the chiral phase observed in the non-reciprocal

Vicsek model [34]. In non-reciprocal systems with discrete symmetry, the chiral phase cannot be realized due to restrictions in particle movement and reduced degrees of freedom. Our investigation further reveals that self-propulsion destroys the oscillatory state obtained for the non-motile case, as also observed in Ref. [35].

Recent studies have argued that liquid polar flocks are metastable to the presence of small obstacles, opposite-polarity droplets, or to the spontaneous nucleation of opposite-phase droplets [16–20]. In this paper, we have also confirmed that for weak diffusivity, the TSAIM long-range polar order or the NRTSAIM run-and-chase states are susceptible to spontaneous droplet nucleation, leading to a variety of steady-state system morphologies. In the TSAIM without species flip, the state is long-range ordered in spin but short-range ordered in species, whereas, in the presence of species flip, the situation is reversed. For the NRTSAIM, the resulting state is characterized by short-range ordered gas. As θ is decreased, the metastability of the HDPF state becomes less pronounced due to an increase in the nucleation time of the droplets. This is a result of the constraint $v \leq 2D/(1 - \theta)$, which requires large diffusion D or small velocities v (see appendix F). Moreover, at sufficiently low temperatures, all three models of TSAIM exhibit a spontaneous motility-induced interface pinning transition (without any impurities or disorder), as first reported in Ref. [20]. This transition prevents the system from evolving into an HDPF state (in TSAIM) or a run-and-chase state (in NRTSAIM) when $\beta_1, \beta_2 \rightarrow \infty$.

In conclusion, our study of the two-species active Ising model (TSAIM) and its non-reciprocal counterpart (NRTSAIM) provides significant insights into the dynamics of multi-species flocking systems. The emergence of complex steady-state phases, shaped by the interplay of diffusion, inter-species dynamics, system size, and non-reciprocal interactions, highlights their profound influence on collective behavior and emphasizes the inherent complexity of active matter systems. We hope our findings will inspire future research into the implications of these dynamics in real-world active matter systems, and further investigations into the effects of heterogeneous environments and external perturbations will provide deeper insights into the stability and adaptability of such systems.

Data Availability

The data that support the findings of this study are available from the corresponding author upon reasonable request.

Code Availability

The codes used in this study are available in Ref. [51].

Acknowledgments

This work was performed with financial support from the German Research Foundation (DFG) within the Collaborative Research Center SFB 1027-A3 and INST 256/539-1.

Author Contributions

MM, SC, JDN, and HR designed the research and discussed the results. MM and SC performed numerical simulations and data analysis. All authors contributed to the writing of the manuscript.

Competing Interests

The authors declare no competing interests.

Appendix A: Derivation of hydrodynamic equations: reciprocal interactions

The time-evolution equation for the number of particles $n_{s,i}^\sigma$ in state σ and species s on site i writes

$$\begin{aligned} \partial_t \langle n_{s,i}^\sigma \rangle &= \sum_{\mathbf{p}} W_{\text{hop}}(\sigma, \mathbf{p}) \langle n_{s,i-p}^\sigma - n_{s,i}^\sigma \rangle \\ &+ \langle n_{s,i}^{-\sigma} W_{\text{flip}}^{(1)}(-\sigma \rightarrow \sigma) - n_{s,i}^\sigma W_{\text{flip}}^{(1)}(\sigma \rightarrow -\sigma) \rangle \\ &+ \langle n_{-s,i}^\sigma W_{\text{flip}}^{(2)}(-s \rightarrow s) - n_{s,i}^\sigma W_{\text{flip}}^{(2)}(s \rightarrow -s) \rangle. \end{aligned} \quad (\text{A1})$$

Noting that

$$n_{s,i-p}^\sigma - n_{s,i}^\sigma = -\mathbf{p} \cdot \nabla n_s^\sigma + \frac{1}{2}(\mathbf{p} \cdot \nabla)^2 n_s^\sigma, \quad (\text{A2})$$

the drift term writes

$$\begin{aligned} I_{\text{hop}} &= \sum_{\mathbf{p}} W_{\text{hop}}(\sigma, \mathbf{p}) [n_{s,i-p}^\sigma - n_{s,i}^\sigma] \\ &= D(1 + \theta\varepsilon) \partial_x^2 n_s^\sigma + D \partial_y^2 n_s^\sigma - 2D\varepsilon\sigma \partial_x n_s^\sigma, \end{aligned} \quad (\text{A3})$$

using the hopping rate $W_{\text{hop}}(\sigma, \mathbf{p})$ given by Eq. (1). We now calculate the expression of the flipping terms:

$$\begin{aligned} I_{\text{flip}}^{(1)} &= n_s^{-\sigma} W_{\text{flip}}^{(1)}(-\sigma \rightarrow \sigma) - n_s^\sigma W_{\text{flip}}^{(1)}(\sigma \rightarrow -\sigma) \\ &= \gamma_1 \left[n_s^{-\sigma} \exp\left(\frac{2\beta_1}{\rho} s \sigma v_a\right) - n_s^\sigma \exp\left(-\frac{2\beta_1}{\rho} s \sigma v_a\right) \right], \end{aligned} \quad (\text{A4})$$

for the spin-orientation σ (with $\beta_1 = \beta J_1$), and

$$I_{\text{flip}}^{(2)} = n_{-s}^\sigma W_{\text{flip}}^{(2)}(-s \rightarrow s) - n_s^\sigma W_{\text{flip}}^{(2)}(s \rightarrow -s) \\ = \gamma_2 \left[n_{-s}^\sigma \exp\left(\frac{2\beta_2}{\rho} sm\right) - n_s^\sigma \exp\left(-\frac{2\beta_2}{\rho} sm\right) \right], \quad (\text{A5})$$

for the species s (with $\beta_2 = \beta J_2$). These flipping terms can be rewritten as

$$I_{\text{flip}}^{(1)} = -\sigma m_s \cosh \frac{2\beta_1 v_a}{\rho} + \sigma s \rho_s \sinh \frac{2\beta_1 v_a}{\rho}, \quad (\text{A6})$$

$$I_{\text{flip}}^{(2)} = -s \mu^\sigma \cosh \frac{2\beta_2 m}{\rho} + s \nu^\sigma \sinh \frac{2\beta_2 m}{\rho}, \quad (\text{A7})$$

with $\rho_s = n_s^+ + n_s^-$, $m_s = n_s^+ - n_s^-$, $\nu^\sigma = n_A^\sigma + n_B^\sigma$, and $\mu^\sigma = n_A^\sigma - n_B^\sigma$. The hydrodynamic equations for density $\rho = \sum_{s\sigma} \langle n_s^\sigma \rangle$, species magnetization $m = \sum_{s\sigma} s \langle n_s^\sigma \rangle$, and order parameters $v_s = \sum_{s\sigma} \sigma \langle n_s^\sigma \rangle$, and $v_a = \sum_{s\sigma} s \sigma \langle n_s^\sigma \rangle$ are:

$$\partial_t \rho = D_{xx} \partial_x^2 \rho + D_{yy} \partial_y^2 \rho - v \partial_x v_s, \quad (\text{A8})$$

$$\partial_t m = D_{xx} \partial_x^2 m + D_{yy} \partial_y^2 m - v \partial_x v_a \\ + 2\gamma_2 \left[\rho \sinh \frac{2\beta_2 m}{\rho} - m \cosh \frac{2\beta_2 m}{\rho} \right], \quad (\text{A9})$$

$$\partial_t v_s = D_{xx} \partial_x^2 v_s + D_{yy} \partial_y^2 v_s - v \partial_x \rho \\ + 2\gamma_1 \left[m \sinh \frac{2\beta_1 v_a}{\rho} - v_s \cosh \frac{2\beta_1 v_a}{\rho} \right], \quad (\text{A10})$$

$$\partial_t v_a = D_{xx} \partial_x^2 v_a + D_{yy} \partial_y^2 v_a - v \partial_x m \\ + 2\gamma_1 \left[\rho \sinh \frac{2\beta_1 v_a}{\rho} - v_a \cosh \frac{2\beta_1 v_a}{\rho} \right] \\ + 2\gamma_2 \left[v_s \sinh \frac{2\beta_2 m}{\rho} - v_a \cosh \frac{2\beta_2 m}{\rho} \right], \quad (\text{A11})$$

with $D_{xx} = D(1 + \theta\varepsilon)$, $D_{yy} = D$, and $v = 2D\varepsilon$. These equations are mean-field expressions such that $\langle f(\cdot) \rangle = f(\langle \cdot \rangle)$. As for the one-species AIM [13], we must consider m and v_a as independent Gaussian variables with variance linear to the density ρ : $\sigma_m^2 = \alpha_m \rho$ and $\sigma_a^2 = \alpha_a \rho$ to observe phase-separated profiles. The hydrodynamic equations, in the refined mean-field approximation, write then:

$$\partial_t \rho = D_{xx} \partial_x^2 \rho + D_{yy} \partial_y^2 \rho - v \partial_x v_s, \quad (\text{A12})$$

$$\partial_t m = D_{xx} \partial_x^2 m + D_{yy} \partial_y^2 m - v \partial_x v_a \\ + 2\overline{\gamma}_2 \left[\left(\rho - \frac{r_2}{2\beta_2} \right) \sinh \frac{2\beta_2 m}{\rho} - m \cosh \frac{2\beta_2 m}{\rho} \right], \quad (\text{A13})$$

$$\partial_t v_s = D_{xx} \partial_x^2 v_s + D_{yy} \partial_y^2 v_s - v \partial_x \rho \\ + 2\overline{\gamma}_1 \left[m \sinh \frac{2\beta_1 v_a}{\rho} - v_s \cosh \frac{2\beta_1 v_a}{\rho} \right], \quad (\text{A14})$$

$$\partial_t v_a = D_{xx} \partial_x^2 v_a + D_{yy} \partial_y^2 v_a - v \partial_x m$$

$$+ 2\overline{\gamma}_1 \left[\left(\rho - \frac{r_1}{2\beta_1} \right) \sinh \frac{2\beta_1 v_a}{\rho} - v_a \cosh \frac{2\beta_1 v_a}{\rho} \right] \\ + 2\overline{\gamma}_2 \left[v_s \sinh \frac{2\beta_2 m}{\rho} - v_a \cosh \frac{2\beta_2 m}{\rho} \right], \quad (\text{A15})$$

with $\overline{\gamma}_i = \gamma_i \exp(r_i/2\rho)$, $r_1 = (2\beta J_1)^2 \alpha_a$, and $r_2 = (2\beta J_2)^2 \alpha_m$.

Appendix B: Derivation of hydrodynamic equations: non-reciprocal interactions

Following the derivation made in Appendix A for reciprocal interactions, we calculate the hydrodynamic equations for the particle density ρ_s , and the magnetization m_s of species s with non-reciprocal interactions:

$$\partial_t \rho_s = D_{xx} \partial_x^2 \rho_s + D_{yy} \partial_y^2 \rho_s - v \partial_x m_s, \quad (\text{B1})$$

$$\partial_t m_s = D_{xx} \partial_x^2 m_s + D_{yy} \partial_y^2 m_s - v \partial_x \rho_s \\ + 2\gamma_1 \left[\rho_s \sinh \frac{2\beta J_{ss'} m_{s'}}{\rho} - m_s \cosh \frac{2\beta J_{ss'} m_{s'}}{\rho} \right], \quad (\text{B2})$$

where the Einstein notation has been used: $J_{ss'} m_{s'} = J_{sA} m_A + J_{sB} m_B$. Since these equations are mean-field expressions, we must consider m_A and m_B as independent Gaussian variables with variance linear to the density ρ : $\sigma_s^2 = \alpha_s \rho$, to observe phase-separated profiles. The hydrodynamic equation for m_s , in the refined mean-field approximation, write then:

$$\partial_t m_s = D_{xx} \partial_x^2 m_s + D_{yy} \partial_y^2 m_s - v \partial_x \rho_s \\ + 2\overline{\gamma}_s \left[\left(\rho_s - \frac{r_{ss}}{2\beta J_{ss}} \right) \sinh \frac{2\beta_1 \mu_s}{\rho} - m_s \cosh \frac{2\beta_1 \mu_s}{\rho} \right], \quad (\text{B3})$$

with $\mu_s = (J_{ss'}/J_1) m_{s'}$, $\overline{\gamma}_s = \gamma_1 \exp[(r_{ss} + r_{s,-s})/2\rho]$, and $r_{ss'} = (2\beta J_{ss'})^2 \alpha_{s'}$. We have considered that the two species have non-reciprocal interactions but are intrinsically the same, we then have $J_{AA} = J_{BB} = J_1$ and $\alpha_A = \alpha_B$. We get then $r_{AA} = r_{BB} \equiv r_1$, $r_{ss'} = (J_{ss'}/J_1)^2 r_1$, and the simplified equation:

$$\partial_t m_s = D_{xx} \partial_x^2 m_s + D_{yy} \partial_y^2 m_s - v \partial_x \rho_s \\ + 2\overline{\gamma}_s \left[\left(\rho_s - \frac{r_1}{2\beta_1} \right) \sinh \frac{2\beta_1 \mu_s}{\rho} - m_s \cosh \frac{2\beta_1 \mu_s}{\rho} \right], \quad (\text{B4})$$

with $\overline{\gamma}_s = \gamma_1 \exp[(r_1 + r_{s,-s})/2\rho]$.

Appendix C: Paramagnetic and ferromagnetic gas phase of the TSAIM with species flip

Fig. 23 shows the morphology of the different gas phases observed in the reciprocal TSAIM with species flip

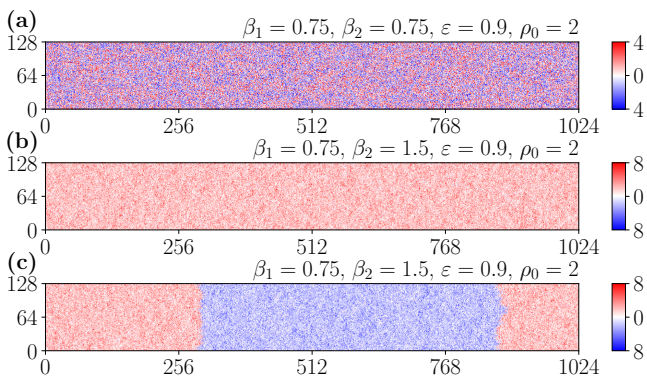


FIG. 23: (color online) Gas phases of the reciprocal TSAIM with species flip ($\gamma_2 = 0.5$), for $\beta_1 = 1.8$, $\varepsilon = 0.9$, $\rho_0 = 2$ in a 1024×128 domain. (a) Paramagnetic gas phase for $\beta_2 = 0.75$. (b–c) Ferromagnetic gas phase for $\beta_2 = 1.5$ starting from two different initial configurations: (b) $m_0 = 2$ and (c) $m_0 = 0$ (colormap as in Fig. 1).

[see Fig. 11(d–f)] as β_2 is varied. For $\beta_2 = 0.75$, the particles are disordered in spin and species [Fig. 23(a)], resulting in zero average local and species magnetizations, $\langle m_{s,i} \rangle = \langle m_i \rangle = 0$, which characterizes the *paramagnetic gas phase*. For $\beta_2 = 1.5$, the particles are disordered in spin but ordered in species [Fig. 23(b–c)], resulting in zero average local magnetization, $\langle m_{s,i} \rangle = 0$, but a positive average species magnetization, $\langle m_i \rangle > 0$, which characterizes the *ferromagnetic gas phase*. Starting with all particles in species A ($m_0 = \rho_0$), a ferromagnetic gas phase of species A is obtained [Fig. 23(b)], whereas starting with an equal population of each species ($m_0 = 0$) distributed into two bands (semi-ordered configuration) leads to a ferromagnetic gas phase with both species occupying half of the space [Fig. 23(c)].

Appendix D: Microphase separation in the coexistence region of the TSAIM with species flip

Fig. 24 shows the density profiles for species A and B as a function of increasing density for $\beta_1 = 1.8$ and $\beta_2 = 0.75$, starting from a disordered configuration. As density increases, we observe the formation of alternating dense bands of species A and B moving in a PF state, with the number and average width of these high-density bands growing as density is increased [Fig. 24(a–e)]. As we further increase ρ_0 , the number of bands initially remains constant [Fig. 24(f–g)], while the average bandwidth increases before the band numbers eventually decrease as the bands become wider [Fig. 24(h)]. These alternating density patterns resemble the traveling bands observed in the Vicsek model, referred to as the *microphase* separation of the coexistence region [10, 33]. However, in the Vicsek model, the microphase-separated bands exhibit a distinctive characteristic: increasing density does not alter the shape or width of these bands,

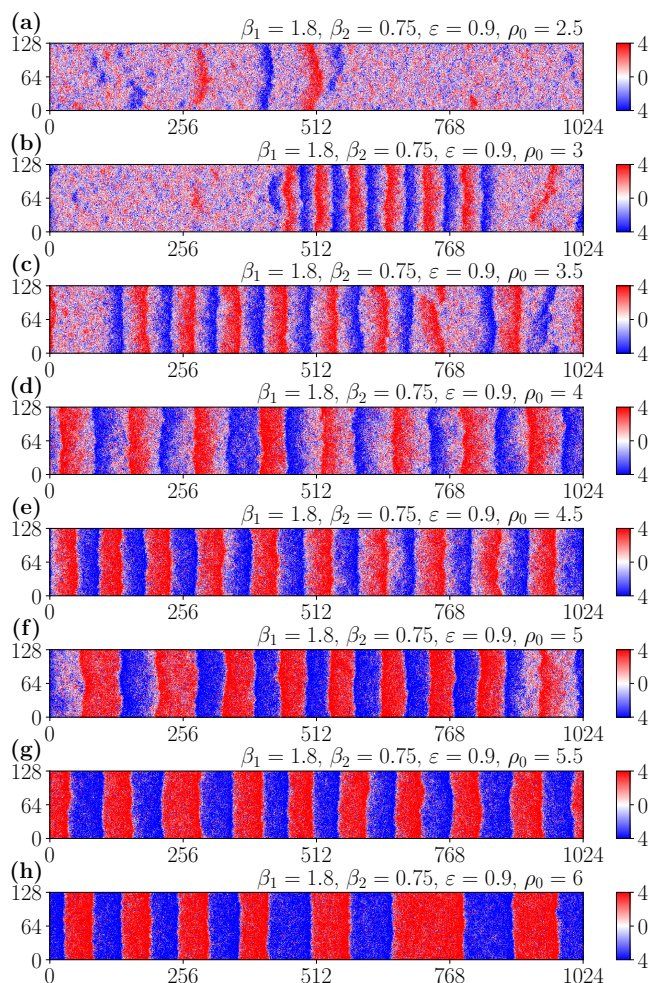


FIG. 24: (color online) Microphase separation in the coexistence region of the TSAIM with species flip ($\gamma_2 = 0.5$). Steady-state density profiles for $\beta_1 = 1.8$, $\beta_2 = 0.75$, $\varepsilon = 0.9$, and increasing density ρ_0 , in a 1024×128 domain, exhibiting alternate bands of species A and B in a PF state (colormap as in Fig. 1).

instead, it only increases the number of bands. Similar patterns also emerge in the PF state of the TSVM [33], but upon increasing density, the system transitions to an APF state. In contrast, here we observe a HDPF state characterized by multiple bands. Another difference between the microphase patterns observed in Fig. 24 and those in the Vicsek model [10] or the TSVM [33] is that, in the VM and TSVM, giant density fluctuations are responsible for the breakdown of large liquid domains. In contrast, in the TSAIM, we observe normal density fluctuations akin to the one-species AIM [13], indicating that fluctuations do not play a similar role here. We should note that, for a fixed density, increasing β_2 while maintaining the condition $\beta_1 > \beta_2$ leads to the destruction of these microphase patterns. This occurs because, with a larger β_2 , particles are more likely to flip their species, resulting in the formation of a single-species flock. Fur-

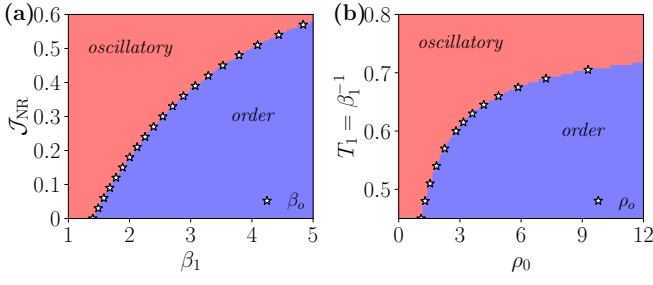


FIG. 25: (color online) (a) $(\mathcal{J}_{\text{NR}}, \beta_1)$ stability diagram for $\rho_0 = 2.5$, and (b) temperature-density stability diagram for $\mathcal{J}_{\text{NR}} = 0.1$, under the condition given by Eq. (E5): stable ordered solution in blue region, and unstable ordered solution in red region. The symbols report here the transition point presented in Figs. 22(e-f).

thermore, the emergence of the *microphase* separation results from a quench starting from a disordered initial condition, and thus, for $\rho_0 > 4.5$, the formation of these multiple bands is not a steady-state property. At higher densities, if we begin with a liquid PF initial condition, the system remains in a bulk phase-separated state.

Appendix E: Oscillatory/order transition line in the non-motile NRTSAIM

In this section, we derive a stability criterion for an ordered solution $(m_{A,0}, m_{B,0})$ following the time evolution dictated by Eq. (21). The stationary magnetizations $m_{A,0}$ and $m_{B,0}$ are solutions of the Eq. (22). We consider a perturbation to this ordered solution as $m_s(t) = m_{s,0} + \delta m_s(t)$. Keeping only the linear terms in δm_s in Eq. (21), we get

$$\frac{\delta \dot{m}_s}{\overline{\gamma}_s} = \left(\beta_1 - \frac{r_1}{\rho_0} \right) \cosh(\kappa \mu_{s,0}) \delta \mu_s - \cosh(\kappa \mu_{s,0}) \delta m_s - \kappa m_{s,0} \sinh(\kappa \mu_{s,0}) \delta \mu_s, \quad (\text{E1})$$

with $\mu_{s,0} = m_{s,0} + \mathcal{J}_{s,-s} m_{-s,0}$, $\delta \mu_s = \delta m_s + \mathcal{J}_{s,-s} \delta m_{-s}$, and $\kappa = 2\beta_1/\rho_0$. This equation can be rewritten in a matrix form $\delta m_s / \overline{\gamma}_s = M_{ss'} \delta m_{s'}$ with the diagonal matrix elements:

$$\begin{aligned} M_{ss} &= \left(\beta_1 - 1 - \frac{r_1}{\rho_0} \right) \cosh(\kappa \mu_{s,0}) - \kappa m_{s,0} \sinh(\kappa \mu_{s,0}), \\ &= \left(\beta_1 - 1 - \frac{r_1}{\rho_0} - \kappa^2 \frac{m_{s,0}^2}{\beta_1 - r_1/\rho_0} \right) \cosh(\kappa \mu_{s,0}), \end{aligned} \quad (\text{E2})$$

and the off-diagonal matrix elements ($s' \neq -s$):

$$\frac{M_{ss'}}{\mathcal{J}_{ss'}} = \left(\beta_1 - \frac{r_1}{\rho_0} \right) \cosh(\kappa \mu_{s,0}) - \kappa m_{s,0} \sinh(\kappa \mu_{s,0}),$$

$$= \left(\beta_1 - \frac{r_1}{\rho_0} \right) \left[1 - \left(\frac{2m_{s,0}}{\rho_0 - r_1/\beta_1} \right)^2 \right] \cosh(\kappa \mu_{s,0}), \quad (\text{E3})$$

where Eq. (22) have been used to simplify the expressions. We denote λ_{\pm} the two eigenvalues of M , and the evolution of the perturbation is dictated by the sign of the real part of

$$\lambda_{\pm} = \frac{M_{AA} + M_{BB}}{2} \pm \frac{1}{2} \sqrt{(M_{AA} - M_{BB})^2 + 4M_{AB}M_{BA}}. \quad (\text{E4})$$

Since the oscillatory/order transition occurs at a larger density than ρ_* , at which the disorder/oscillation occurs, we have then $\beta_1 - r_1/\rho_0 \leq 1$; and Eq. (22) tells us that $m_{s,0} < \rho_0/2 - r_1/2\beta_1$. The right-hand side of Eq. (E3) is thus strictly positive, and $M_{ss'}$ has the same sign as $\mathcal{J}_{ss'}$, i.e. the product $M_{AB}M_{BA}$ is negative for the non-reciprocal interactions we are considering here. From the general form of the eigenvalues of M , given by Eq. (E4), we get then the inequalities: $\min(M_{AA}, M_{BB}) \leq \lambda_- \leq \lambda_+ \leq \max(M_{AA}, M_{BB})$, meaning that the ordered solution remains stable as soon as M_{AA} and M_{BB} are negative. From Eq. (E2), and considering $\rho_0 > \rho_*$, M_{ss} is negative if and only if the magnetization $m_{s,0}$ satisfies the inequality

$$m_{s,0}^2 \geq \left(\frac{\rho_0}{2} - \frac{\rho_0 + r_1}{2\beta_1} \right) \left(\frac{\rho_0}{2} - \frac{r_1}{2\beta_1} \right). \quad (\text{E5})$$

Fig. 25 shows the stability diagrams computed as follows: we consider the series of N magnetization values $\{m_{s,n}\}_{n \in \{1, N\}}$ defined by

$$m_{s,n+1} = \left(\frac{\rho_0}{2} - \frac{r_1}{2\beta_1} \right) \tanh \frac{2\beta_1 \mu_{s,n}}{\rho_0}, \quad (\text{E6})$$

with $\mu_{s,n} = m_{s,n} + \mathcal{J}_{s,-s} m_{-s,n}$ and $m_{s,1} = \rho_0/2$. If the first $N = 1000$ elements satisfy the condition given in Eq. (E5), then the ordered solution $m_{s,0} = \lim_{n \rightarrow \infty} m_{s,n}$ is stable, otherwise no ordered solution is reached. These stability diagrams are consistent with the numerical solutions of Eq. (21) shown in Figs. 22(e-f), and reported with symbols on Fig. 25.

Appendix F: Metastability in the reciprocal TSAIM without species flip for $\theta < 1$

In Sec. IV B, we have demonstrated that the HDPF state is vulnerable to spontaneous droplet nucleation, analogously to the one-species AIM [20], under the hopping rate W_{hop} with $\theta = 1$, resulting in a transition to a state that is long-range ordered in spin but short-range ordered in species [see Fig. 5(b)]. Fig. 26 shows the density profile after $t_{\text{max}} = 1.5 \times 10^5$ MCS, starting from an HDPF state for varying $\theta < 1$, where the inequality $v \leq 2D/(1 - \theta)$ should be considered (see Sec. II). At

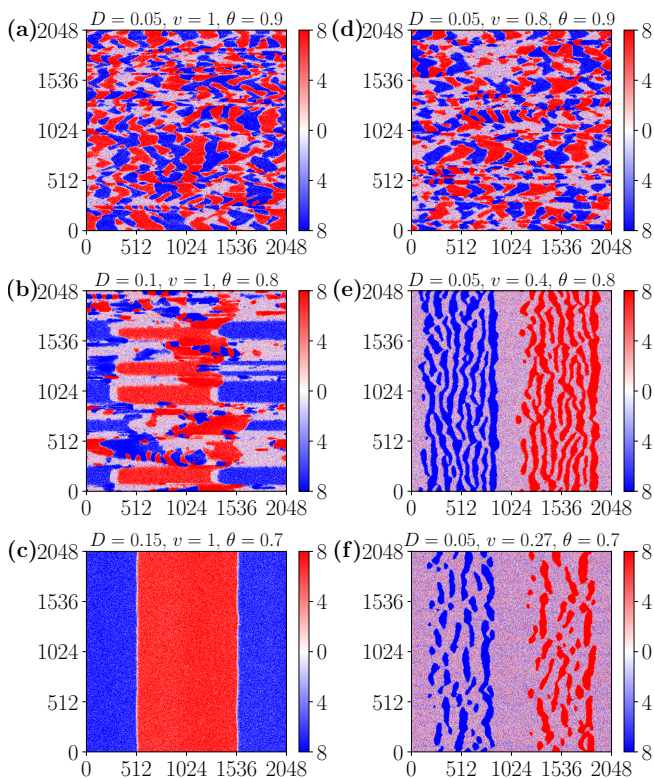


FIG. 26: (color online) Metastability in the reciprocal TSAIM without species flip ($\gamma_2 = 0$). Snapshots after 1.5×10^5 MCS for $\beta_1 = 1$, $\rho_0 = 8$, and varying $\theta < 1$ in a 2048×2048 domain, (a–c) for $v = 1$ and varying D , and (d–f) for $D = 0.05$ and varying v (colormap as in Fig. 1).

fixed $v = 1$, the diffusion is varied as $D = (1 - \theta)/2$

[Fig. 26(a–c)]; while at fixed $D = 0.05$, the velocity is changed as $v = 0.08/(1 - \theta)$ [Fig. 26(d–f)]. These snapshots at fixed time t_{\max} allow us to determine how the spontaneous droplet nucleation behaves with θ . For $\theta = 0.9$, Fig. 26(a,d) shows a breakdown of the HDPF state leading to the formation of a new steady-state similar to $\theta = 1$, shown in Fig. 5(b). For $\theta = 0.8$, the further increase of D (at fixed $v = 1$) makes the droplet nucleation process less frequent, and the resulting HDPF state exhibits larger correlation lengths [Fig. 26(b)]. However, the decrease of v (at fixed $D = 0.05$) shows no spontaneous droplet excitation after a time t_{\max} , and the resulting state presents elongated liquid domains [Fig. 26(e)], analogous to a quench of a liquid state into the coexistence region of the one-species AIM [13]. For $\theta = 0.7$, the increase of D significantly raises the droplet nucleation time, rendering it inaccessible after the time t_{\max} , and allowing the initial HDPF state to persist [Fig. 26(c)]. Conversely, the decrease of v slows down particle movement considerably, leading to fewer but much denser elongated liquid domains [Fig. 26(f)]. Further decreasing of θ will require an additional increase of D (for fixed $v = 1$) or a decrease of v (for fixed $D = 0.05$), yielding an absence of spontaneous droplet nucleation after a time t_{\max} . This mainly shows that the spontaneous droplet nucleation time, increasing with D and decreasing with v , mainly decreases with θ due to the inequality $v \leq 2D/(1 - \theta)$. The influence of decreasing θ in the reciprocal TSAIM with species flip is analogous. For $\theta = 0.9$, we observe a steady state characterized by short-range order in spin, similar to Fig. 12(b), while the spontaneous droplet nucleation time increases for smaller values of θ .

-
- [1] M. C. Marchetti, J. F. Joanny, S. Ramaswamy, T. B. Liverpool, J. Prost, M. Rao, and R. A. Simha, *Hydrodynamics of soft active matter*, Rev. Mod. Phys. **85**, 1143 (2013).
- [2] S. Ramaswamy, *The mechanics and statistics of active matter*, Annu. Rev. Condens. Matter Phys. **1**, 323 (2010); *Active matter*, J. Stat. Mech.: Theor. Exp. 054002 (2017).
- [3] G. de Magistris and D. Marenduzzo, *An introduction to the physics of active matter*, Physica A **418**, 65 (2015).
- [4] C. Bechinger, R. di Leonardo, H. Löwen, C. Reichhardt, G. Volpe, and G. Volpe, *Active particles in complex and crowded environments*, Rev. Mod. Phys. **88**, 045006 (2016).
- [5] M. R. Shaebani, A. Wysocki, R. G. Winkler, G. Gompper, and H. Rieger, *Computational models for active matter*, Nat. Rev. Phys. **2**, 181 (2020).
- [6] M. J. Bowick, N. Fakhri, M. C. Marchetti, and S. Ramaswamy, *Symmetry, thermodynamics, and topology in active matter*, Phys. Rev. X **12**, 010501 (2022).
- [7] S. Strogatz, *Sync: The Emerging Science of Spontaneous Order* (Penguin, London, 2004).
- [8] T. Vicsek, A. Czirók, E. Ben-Jacob, I. Cohen and O. Shochet, *Novel Type of Phase Transition in a System of Self-Driven Particles*, Phys. Rev. Lett. **75**, 1226 (1995).
- [9] F. Ginelli, *The physics of the Vicsek model*, Eur. Phys. J. Special Topics **225**, 2099 (2016).
- [10] A. P. Solon, H. Chaté, and J. Tailleur, *From phase to microphase separation in flocking models: The essential role of nonequilibrium fluctuations*, Phys. Rev. Lett. **114**, 068101 (2015).
- [11] A. P. Solon, J. B. Caussin, D. Bartolo, H. Chaté, and J. Tailleur, *Pattern formation in flocking models: A hydrodynamic description*, Phys. Rev. E **92**, 062111 (2015).
- [12] J. Toner and Y. Tu, *Long-Range Order in a Two-Dimensional Dynamical XY Model: How Birds Fly Together*, Phys. Rev. Lett. **75**, 4326 (1995); *Flocks, herds, and schools: A quantitative theory of flocking*, Phys. Rev. E **58**, 4828 (1998); *J. Toner, Reanalysis of the hydrodynamic theory of fluid, polar-ordered flocks*, Phys. Rev. E **86**, 031918 (2012).
- [13] A. P. Solon and J. Tailleur, *Revisiting the Flocking*

- Transition Using Active Spins*, Phys. Rev. Lett. **111**, 078101 (2013); *Flocking with discrete symmetry: The two-dimensional active Ising model*, Phys. Rev. E **92**, 042119 (2015).
- [14] M. Mangeat, S. Chatterjee, R. Paul, and H. Rieger, *Flocking with a q-fold discrete symmetry: Band-to-lane transition in the active Potts model*, Phys. Rev. E **102**, 042601 (2020); S. Chatterjee, M. Mangeat, R. Paul, and H. Rieger, *Flocking and reorientation transition in the 4-state active Potts model*, EPL **130**, 66001 (2020).
- [15] S. Chatterjee, M. Mangeat, and H. Rieger, *Polar flocks with discretized directions: The active clock model approaching the Vicsek model*, EPL **138**, 41001 (2022); A. Solon, H. Chaté, J. Toner, and J. Tailleur, *Susceptibility of polar flocks to spatial anisotropy*, Phys. Rev. Lett. **128**, 208004 (2022).
- [16] J. Codina, B. Mahault, H. Chaté, J. Dobnikar, I. Pagonabarraga, and X.-q. Shi, *Small obstacle in a large polar flock*, Phys. Rev. Lett. **128**, 218001 (2022).
- [17] M. Karmakar, S. Chatterjee, R. Paul and H. Rieger, *Consequence of anisotropy on flocking: the discretized Vicsek model*, New J. Phys. **26**, 043023 (2024).
- [18] M. Besse, H. Chaté, and A. Solon, *Metastability of Constant-Density Flocks*, Phys. Rev. Lett. **129**, 268003 (2022).
- [19] B. Benvegnen, O. Granek, S. Ro, R. Yaacoby, H. Chaté, Y. Kafri, D. Mukamel, A. Solon, and J. Tailleur, *Metastability of discrete-symmetry flocks*, Phys. Rev. Lett. **131**, 218301 (2023).
- [20] C. U. Woo and J. D. Noh, *Motility-Induced Pinning in Flocking System with Discrete Symmetry*, Phys. Rev. Lett. **133**, 188301 (2024).
- [21] G. R. Graves and N.J. Gotelli, *Assembly of avian mixed-species flocks in Amazonia*, PNAS **90**, 1388, (1993); A. J. W. Ward, T. M. Schaerf, A. L. J. Burns, J. T. Lizier, E. Crosato, M. Prokopenko, and M. M. Webster, *Cohesion, order and information flow in the collective motion of mixed-species shoals*, R. Soc. open sci. **5**, 181132 (2018).
- [22] G. Ariel, O. Rimer, and E. Ben-Jacob, *Order-disorder phase transition in heterogeneous populations of self-propelled particles*, J. Stat. Phys. **158**, 579 (2015).
- [23] S. Peled, S. D. Ryan, S. Heidenreich, M. Bär, G. Ariel, and A. Be'er, *Heterogeneous bacterial swarms with mixed lengths*, Phys. Rev. E **103**, 032413 (2021).
- [24] W. Zuo and Y. Wu, *Dynamic motility selection drives population segregation in a bacterial swarm*, PNAS **117**, 4693 (2020).
- [25] A. Jose, G. Ariel, and A. Be'er, *Physical characteristics of mixed-species swarming colonies*, Phys. Rev. E **105**, 064404 (2022).
- [26] A. M. Menzel, *Collective motion of binary self-propelled particle mixtures*, Phys. Rev. E **85**, 021912 (2012).
- [27] S. R. McCandlish, A. Baskaran, and M. F. Hagan, *Spontaneous segregation of self-propelled particles with different motilities*, Soft Matter **8**, 2527 (2012); S. Mishra, K. Tunström, I. D. Couzin, and C. Huepe, *Collective dynamics of self-propelled particles with variable speed*, Phys. Rev. E **86**, 011901 (2012).
- [28] G. Netzer, Y. Yarom, and G. Ariel, *Heterogeneous populations in a network model of collective motion*, Physica A **530**, 121550 (2019).
- [29] G. Book, C. Ingham, and G. Ariel, *Modeling cooperating micro-organisms in antibiotic environment*, Plos One **12**, e0190037 (2017).
- [30] K. Copenhagen, D. A. Quint, and A. Gopinathan, *Self-organized sorting limits behavioral variability in swarms*, Sci. Rep. **6**, 31808 (2016); V. Khodygo, M. T. Swain, and A. Mughal, *Homogeneous and heterogeneous populations of active rods in two-dimensional channels*, Phys. Rev. E **99**, 022602 (2019); P. K. Bera and A. K. Sood, *Motile dissenters disrupt the flocking of active granular matter*, Phys. Rev. E **101**, 052615 (2020).
- [31] N. A. Mecholsky, E. Ott, and T. M. Antonsen Jr., *Obstacle and predator avoidance in a model for flocking*, Physica D **239**, 988 (2010).
- [32] A. Sengupta, T. Kruppa, and H. Löwen, *Chemotactic predator-prey dynamics*, Phys. Rev. E **83**, 031914 (2011).
- [33] S. Chatterjee, M. Mangeat, C. U. Woo, H. Rieger, and J. D. Noh, *Flocking of two unfriendly species: The two-species Vicsek model*, Phys. Rev. E **107**, 024607 (2023).
- [34] M. Fruchart, R. Hanai, P. B. Littlewood, and V. Vitelli, *Non-reciprocal phase transitions*, Nature **592**, 363 (2021).
- [35] D. Martin, D. Seara, Y. Avni, M. Fruchart, and V. Vitelli, *The transition to collective motion in nonreciprocal active matter: coarse graining agent-based models into fluctuating hydrodynamics*, arXiv:2307.08251 (2024).
- [36] A. V. Ivlev, J. Bartnick, M. Heinen, C.-R. Du, V. Nosenko, and H. Löwen, *Statistical mechanics where Newton's third law is broken*, Phys. Rev. X **5**, 011035 (2015).
- [37] Z. You, A. Baskaran, and M. C. Marchetti, *Nonreciprocity as a generic route to traveling states*, PNAS **117**, 19767 (2020).
- [38] S. Saha, J. Agudo-Canalejo, and R. Golestanian, *Scalar active mixtures: The nonreciprocal Cahn-Hilliard model*, Phys. Rev. X **10**, 041009 (2020).
- [39] H. Hong and S. H. Strogatz, *Kuramoto model of coupled oscillators with positive and negative coupling parameters: an example of conformist and contrarian oscillators*, Phys. Rev. Lett. **106**, 054102 (2011).
- [40] D. Golomb and D. Hansel, *The number of synaptic inputs and the synchrony of large, sparse neuronal networks*, Neural Comput. **12**, 1095 (2000).
- [41] C. Börgers and N. Kopell, *Synchronization in networks of excitatory and inhibitory neurons with sparse, random connectivity*, Neural Comput. **15**, 509 (2003).
- [42] L. Xiong, Y. Cao, R. Cooper, W. J. Rappel, J. Hasty and L. Tsimring, *Flower-like patterns in multi-species bacterial colonies*, eLife **9**, e48885 (2020).
- [43] E. Theveneau, B. Steventon, E. Scarpa, S. Garcia, X. Trepast, A. Streit and R. Mayor, *Chase-and-run between adjacent cell populations promotes directional collective migration*, Nat. Cell Biol. **15**, 763 (2013).
- [44] C. H. Meredith, P. G. Moerman, J. Groenewold, Yu-Jen Chiu, W. K. Kegel, A. van Blaaderen and L. D. Zarzar, *Predator-prey interactions between droplets driven by non-reciprocal oil exchange*, Nat. Chem. **12**, 1136 (2020).
- [45] S. A. M. Loos and S. H. L. Klapp, *Irreversibility, heat and information flows induced by non-reciprocal interactions*, New J. Phys. **22**, 123051 (2020).
- [46] M. Durve and A. Sayeed, *First-order phase transition in a model of self-propelled particles with variable angular range of interaction*, Phys. Rev. E **93**, 052115 (2016).
- [47] M. Durve, A. Saha, and A. Sayeed, *Active particle condensation by non-reciprocal and time-delayed interactions*, Eur. Phys. J. E **41**, 49 (2018).
- [48] J. Ashkin and E. Teller, *Statistics of Two-Dimensional Lattices with Four Components*, Phys. Rev. **64**, 178

- (1943).
- [49] C. Fan, *On critical properties of the Ashkin-Teller model*, Physics Letters A **39**, 136 (1972).
- [50] R. V. Ditzian, J. R. Banavar, G. S. Grest, and L. P. Kadanoff, *Phase diagram for the Ashkin-Teller model in three dimensions*, Phys. Rev. B **22**, 2542 (1980); F. A. da Costa, M. J. de Oliveira, and S. R. Salinas, *Asymmetric Baxter phase in the symmetric Ashkin-Teller model*, Phys. Rev. B **36**, 7163 (1987).
- [51] M. Mangeat, S. Chatterjee, J. D. Noh, and H. Rieger, *Codes for “Emergent complex phases in a discrete flocking model with reciprocal and non-reciprocal interactions”*, Zenodo, <https://doi.org/10.5281/zenodo.14257074> (2024).
- [52] W. H. Press, *Numerical recipes: The art of scientific computing* (Cambridge University Press, Cambridge, UK, 2007).
- [53] R. Courant, K. Friedrichs, and H. Lewy, *Über die partiellen Differenzgleichungen der mathematischen Physik*, Math. Ann. **100**, 32–74 (1928).
- [54] M. Mangeat, S. Chatterjee, J. D. Noh, and H. Rieger, *Supplementary movies for “Emergent complex phases in a discrete flocking model with reciprocal and non-reciprocal interactions”*, Zenodo, <https://doi.org/10.5281/zenodo.14261008> (2024).
- [55] K. Binder, *Applications of Monte Carlo methods to statistical physics*, Rep. Prog. Phys. **60**, 487 (1997).
- [56] S. Basu, S. Majumder, S. Sutradhar, S. K. Das and R. Paul, *Phase segregation in a binary fluid confined inside a nanopore*, EPL **116**, 56003 (2016).
- [57] S. K. Baek, P. Minnhagen, and B. J. Kim, *True and quasi-long-range order in the generalized q-state clock model*, Phys. Rev. E **80**, 060101(R) (2009).
- [58] Y. Avni, M. Fruchart, D. Martin, D. Seara, and V. Vitelli, *The non-reciprocal Ising model*, arXiv:2311.05471 (2024).